Journal of Molecular Liquids 438 (2025) 128749

Contents lists available at ScienceDirect

Journal of Molecular Liquids

journal homepage: www.elsevier.com/locate/molliq

Cu-modified $B_{12}N_{12}$ nanocages as efficient carriers for allopurinol drug delivery: Insights from DFT

Mohammad A. Matin [a,*], Md. Abdur Rahman [a], Joyanta K. Saha [b], Joonkyung Jang [c]

[a] Computing Research Laboratory, Centre for Advanced Research in Sciences (CARS), Dhaka University, Dhaka 1000, Bangladesh
[b] Department of Chemistry, Jagannath University, Dhaka 1100, Bangladesh
[c] Department of Nanoenergy Engineering, Pusan National University, Busan 46241, Republic of Korea

ARTICLE INFO

Keywords:
Cu-modified $B_{12}N_{12}$ nanocage
Allopurinol
Hyperuricemia
Chemisorption's
Density functional theory (DFT)
Transition metal

ABSTRACT

Nanostructured materials are widely used in biomedical applications due to their small size, high surface area, and effectiveness in drug delivery. This study investigates Cu-modified $B_{12}N_{12}$ nanocages as carriers for the allopurinol (APN) drug using density functional theory (DFT) at the B3LYP-GD3(BJ)/6-31G(d,p) level. Five Cu-modified structures: $CuB_{11}N_{12}$ and $B_{12}N_{11}Cu$ (doped nanocages), Cu@b64 and Cu@b66 (decorated nanocages), and $Cu@B_{12}N_{12}$ (encapsulated nanocage) were optimized and analyzed. Adsorption energies, electronic and thermodynamic properties (ΔG and ΔH), NBO, PDOS, QTAIM, and non-covalent interactions (NCI) were examined to understand APN-nanocage interactions. APN acts as a charge donor, while the nanocages act as charge acceptors, with adsorption energies ranging from −22.11 to −39.08 kcal·mol^{-1}, indicating weak chemisorption. Among the studied systems, Cu@b66 showed the highest transport potential, remarkable electronic sensitivity ($\Delta E_{gap} = 58.21$ %), and acceptable recovery times (120.01 ms–30.01 s). Adsorption reduced the HOMO-LUMO gap (**1.01–2.62 eV**) and chemical hardness, promoting electron transport (~0.35 e). Acidic condition simulations demonstrated pH-responsive APN release via protonation. These results suggest that Cu-modified $B_{12}N_{12}$ nanocages are promising candidates for efficient and controlled APN delivery. This study provides insights into designing novel nanocarriers based on Cu-modified and pure $B_{12}N_{12}$ nanocages for APN drug delivery applications.

1. Introduction

Allopurinol, with a chemical formula of $C_5H_4N_4O$, resembles the natural purine hypoxanthine in the human body [1,2]. This synthesis was documented in 1956 by G. B. Elion and G. H. Hitchings during their investigate the antineoplastic agents [3].The most stable tautomer of allopurinol is the 1,5-dihydro-4H-pyrazolo pyrimidin-4-one [4]. Allopurinol and its active metabolite, oxypurinol, function as inhibitors of xanthine oxidase enzyme, crucial in purine catabolism, thus, hypoxanthine and xanthine cannot be converted to uric acid [5,6].First approved by the US FDA in 1966 under the trade name Zyloprim, allopurinol is prescribed for conditions such as hyperuricemia, gout, recurrent urates, kidney stones, and as a preventive measure during cancer chemotherapy [7]. Despite its effectiveness in controlling uric acid levels, allopurinol is linked to adverse effects on the human body due to the formation of oxypurinol through oxidation within about two hours of oral administration, with oxypurinol being the main contributor to these adverse effects [1,8]. Some of the most concerning adverse reactions include hypersensitivity syndrome (HSS), Stevens–Johnson syndrome (SJS), and toxic epidermal necrolysis (TEN) [9].Studies have demonstrated that allopurinol is a primary cause of HSS, SJS, or TEN across diverse populations worldwide, including Pacific-Asian, European, and Israeli demographics [10]. Despite the risks, allopurinol remains a crucial treatment option for severe medical conditions. However, its potential adverse effects warrant careful monitoring and strict regulations to mitigate associated risks. Extensive research endeavors aim to design drugs and develop innovative techniques for controlled drug delivery to targeted sites [11]. Therefore, precise administration of drugs at specific concentrations and effective sites is crucial for optimal therapeutic outcomes, necessitating extensive exploration in the development of drug delivery carriers to achieve efficient delivery to targeted cells [12]. A diverse range of drug-delivery vehicles has been employed for drug transfer, but nanoparticles have brought about a significant revolution, especially in targeted drug delivery for anticancer drugs. Nanoparticles

* Corresponding author.
E-mail addresses: matin123@du.ac.bd (M.A. Matin), arahman@du.ac.bd (Md.A. Rahman), jkjang@pusan.ac.kr (J. Jang).

https://doi.org/10.1016/j.molliq.2025.128749
Received 26 March 2025; Received in revised form 14 October 2025; Accepted 16 October 2025
Available online 21 October 2025

act as highly efficient drug-delivery carriers due to their large surface area and small size, enabling easy penetration through cell barriers [13]. Carbon nanotubes, fullerenes, and boron nitride fullerenes, among other nanostructures, have undergone computational and experimental studies to evaluate their drug-delivery potential. Their small dimensions allow easy conjugation with drug molecules [14]. Moreover, their surface properties and non-toxic nature enable targeted delivery without harming healthy cells, making them valuable as drug-delivery vehicles.

Nanomaterials play an essential role in the area of nanoscience and nanotechnology, because of their exceptional characteristics such as optical, magnetic and electric properties [15]. Their wide range of uses in areas like healthcare, electronics, and the chemical sector has garnered significant research attention [16]. Their versatility has led to a growing demand for advanced, cost-effective sensing materials capable of detecting and mitigating the adverse effects of drugs like APN [17]. With their high adsorption capacity, excellent sensing performance, rapid detection capabilities, and compact electronic structures, they are considered ideal candidates for these applications [18,19]. Boron nitride ($B_{12}N_{12}$) nanostructures have garnered much of interest from scholars due to their exceptional physicochemical properties, making them advantageous for drug-delivery carriers [20]. The inorganic nature of $B_{12}N_{12}$, with its high chemical and thermal stability, wide band gap, and strong mechanical strength, makes it a favorable candidate for drug delivery applications [21,22]. Moreover, the non-toxic nature of $B_{12}N_{12}$ fullerenes, reported as early as 2009, underscores their suitability for medical science applications [23]. The stability of $B_{12}N_{12}$ nanostructures results from the ionic bond among the positively charged B atom and negatively charged N atom, enabling bonding with other molecules. These unique attributes have prompted scientific investigation into their potential applications in nanomedicine, biomedical science, and drug interactions [24].

Various fullerene-like $B_{12}N_{12}$ nanostructures, including $B_{10}N_{10}$, $B_{12}N_{12}$, $B_{24}N_{24}$, and $B_{28}N_{28}$, exist, with $B_{12}N_{12}$ being the most stable structure [24,25]. Boron nitride nanocages, especially small fullerene-like structures like $B_{12}N_{12}$, are highly stable and well-suited for biosensing purposes [26]. The detection efficiency of these architectures can be further improved by incorporating transition metal atoms through doping [27,28]. Jensen and Toftlundt demonstrated the structural robustness of $B_{12}N_{12}$ nanostructures, identifying six tetragonal and eight hexagonal rings in four potential configurations using HF and MP2 methods [25]. Subsequent theoretical studies further confirmed the stability of the $B_{12}N_{12}$ nanocage [29,30]. Oku et al. [31] experimentally fabricated the $B_{12}N_{12}$ nanocage using arc-melting, confirming the previous theoretical predictions [25,30,32]. A lot of investigations have been devoted to the synthesis of fullerene-like boron nitride nanocages [33,34]. Among these, Zhu et al. [35] successfully produced $B_{12}N_{12}$ nanocages in large quantities using a custom B–N–O precursor.

Numerous research groups have explored the effects of stature and doping on nanomaterials, focusing on their drug-carrying efficiency and physicochemical characteristics for improve device capabilities. For example, Muz et al. studied the sensing, electronic and optical properties of boron nitride nanostructures, highlighting how these properties vary with diameter and size [36,37]. Evaluating the cytotoxicity of nanomaterials is critical for their application in biological systems. Recent studies have shown that carbon and BN nanostructures exhibit promising cytotoxicity and biocompatibility [38,39].

Density functional theory (DFT) has been used extensively to study boron nitrides and drugs, such as allopurinol (APN) [40]. Cao et al. investigated the adsorption properties of penicillamine drug on pristine $B_{12}N_{12}$ nanocages through DFT calculations, evaluating how it responds in solvents such as water and chloroform. Their findings indicated that the drug chemisorbs onto the nanocages, showing high reactivity and conductivity, supported by thermodynamic analyses [41]. Hazrati and Hadipour investigated the effect of B, Si and Al doping on fullerene C60 to the binding of 5-fluorouracil (5-FU), offering significant insights into their adsorption characteristics [42]. Extensive theoretical and experimental research has explored the adsorption of pharmaceutical drugs onto BN nanomaterials, emphasizing their wide range of potential applications [43]. For instance, research on 5-Aminolevulinic acid (5-ALA) using nanocages $B_{12}N_{12}$ and $B_{16}N_{16}$ offered insights into their potential for drug delivery [44]. Ibrahim et al. explored the delivery of drugs and sensing abilities of $Be_{12}O_{12}$ and $B_{12}N_{12}$ nanocages for APN [45], while Saadh et al. evaluated iron-doped $B_{12}N_{12}$ fullerene nanocages as efficient transporters for the APN drug [46]. Guo et al. performed both theoretical and experimental studies on BN nanomaterials and their doped variants, highlighting their capability for melphalan adsorption and sensing [47]. Additionally, $B_{12}N_{12}$ and its derivatives have demonstrated the ability to absorb a variety of drugs, including 5-Fluorouracil [48], sulphoraphane [49], Sulfasalazine [50], 6-Thioguanine [51], Flucytosine [52], Emodin [53], Naproxen [54], Serine [55], Fluoroquinolone [56], Metformin [57], Chlormethine [58], Azacitidine [59], Mercaptopyridine [60], Curcumin [61], Penicillamine [62], Favipiravir [63,64], Alprazolam [65], Allopurinol [40,45,46], Hydroxyurea [66], 1,3,4-Oxadiazole [67], Gemifloxacin [68], Temozolomide [69], Procarbazine [70], Ifosfamide [71], Thalidomide [72], gemcitabine [73], Sulfasalazine [74], Carmustine [75], and Nitrosourea [76].

These findings emphasize the significant potential of nanocage clusters in biomedical applications, including biosensing, bioimaging, and the targeted delivery of therapeutic agents.

The type of the APN drug's intermolecular interactions with Cu-modified $B_{12}N_{12}$ nanocages play a crucial role in the effectiveness of the drug delivery system, facilitating efficient drug adsorption and controlled release. The APN drug binds strongly to the nanocages through key interactions. The stability of the attachment is governed by the hydrogen bonding, van der Waals (vdW) forces, and electrostatic attractions. This firm binding is vital for the efficient movement of the drug to its targeted sites. The adsorption and deformation energies are also affected by these interactions, and they exhibit positive values, suggesting a degree of structural deformation. Gaining a deeper insight into these interactions can enhance the effectiveness and efficiency of the drug delivery system, resulting in improved therapeutic results.

The adsorption of APN with late transition metal, such as copper modified $B_{12}N_{12}$ fullerenes has not yet been studied, despite significant progress. Despite tremendous advancements, there is currently no research on the adsorption of APN with late transition metals, such as copper modified $B_{12}N_{12}$ fullerenes. Usually, early transition metals have a substantial binding affinity for these surfaces, complicating their detachment. In comparison, late transition metals such as copper show a relatively weaker binding strength, making them suitable for such applications. Previous research has shown that Cu-modified nanocages, including doped configurations ($CuB_{11}N_{12}$ and $B_{12}N_{11}Cu$), decorated structures (Cu@b64 and Cu@b66), and the encapsulated fashion ($Cu@B_{12}N_{12}$), are energetically stable [64,77]. These findings inspired the establishment of a system using Cu-modified $B_{12}N_{12}$ nanocages to effectively bind APN and assist in its elimination from harmful environments.

This study investigates materials with superior APN drug transport and sensing properties, emphasizing pristine and Cu-modified $B_{12}N_{12}$ nanocages in gas and aqueous phase. The $B_{12}N_{12}$ structure was strategically modified by integrating Cu metal through doping, surface decoration, and encapsulation approaches. Density functional theory (DFT) was employed to comprehensively investigate the structural, electronic, adsorption, and thermodynamic characteristics, aiming to identify an effective carrier for the APN drug. The findings of this research offer valuable insights for future development of nanomaterial-based drug carriers and sensors, with potential applications regarding the allopurinol drug.

2. Computational details

This study used the B3LYP-GD3(BJ) functional group to optimize the

geometry of the drug APN and the Cu-modified $B_{12}N_{12}$ nanocagesusing the 6-31G(d,p) basis set within the DFT framework, as implemented in the Gaussian 16 program [78]. We specifically employed the B3LYP-GD3(BJ) functional with the combination of basis set 6-31G(d,p), a well-established and reliable method commonly used for nanocluster investigations.

The modification of $B_{12}N_{12}$ with copper resulted in five optimized structures: doped ($CuB_{11}N_{12}$ and $B_{12}N_{11}Cu$, introducing a Cu atom rather than B and N atom, accordingly), decorated nanocages (Cu@b64 and Cu@b66, where the Cu atom is placed on top of the atomic bond connecting a hexagonal ring to tetragonal ring and another linking two hexagonal rings, correspondingly), and the encapsulated fashion nanocage ($Cu@B_{12}N_{12}$, where one Cu atom is housed inside the nanocage of $B_{12}N_{12}$) structures. The structures under consideration were kept as neutral entities with a total charge of zero. Stabilization was achieved by employing a singlet spin state (M = 2S + 1, in which S represents the total spin) for the $B_{12}N_{12}$, $CuB_{11}N_{12}$, and $B_{12}N_{11}Cu$ nanocages, whereas a spin with doublet spin was utilized for the nanocages Cu@b64, Cu@b66 and the $Cu@B_{12}N_{12}$, respectively. To confirm the local minimum structures in the ground state, the vibrational frequencies were estimated. The optimized nanocages reflect the actual local minima structures, as verified by the lack of imaginary frequencies(see Table S3).

To assess the structural stability of the nanocages, cohesive energy (E_{coh}) was computed using Eq. 1; [53].

$$E_{coh} = \frac{1}{P}\left(E_{nanocage} - xE_B - yE_N - zE_{Cu}\right) \quad (1)$$

The cohesive energy (E_{coh}) was calculated applying the total energy of the nanocage ($E_{nanocage}$), along with the individual energies of the atoms B, N, and Cu (E_B, E_N, and E_{Cu}), where B, N and Cu atoms within the nanocages are represented by x, y and z, and P denotes the total atoms of the nanocages. Particularly, z = 0 indicates the pristine structures, whereas z = 1 represents structures modified with Cu. The HOMO-LUMO energy gap (E_g) is defined as Eq. (2);

$$E_g = E_{LUMO} - E_{HOMO} \quad (2)$$

The energy gap (E_g), is determined as the difference of the lowest unoccupied molecular orbital (LUMO) and the highest occupied molecular orbital HOMO), serves as a crucial factor determining reactivity and electronic properties. The electronic sensitivity (ΔE_g) for the interaction between the APN drug and the $B_{12}N_{12}$ or $B_{12}N_{12}$ nanocages modified with Cu were computed using Eq. 3;

$$\Delta E_g(\%) = \left[\frac{\left(E_{g(nanocage-APN)} - E_{g(nanocage)}\right)}{E_{g(nanocage)}}\right] \times 100 \quad (3)$$

$E_{g(nanocage\text{-}APN)}$ represents the energy gap of $B_{12}N_{12}$-APNor Cu-$B_{12}N_{12}$-APN complexes, E_g(nanocage) represents the energy gap of $B_{12}N_{12}$ or Cu-modified $B_{12}N_{12}$ nanocages accordingly.

The adsorption energy (E_{ads}) was determined using the Eq. 4 to assess the interaction strength between anticancer drugs and $B_{12}N_{12}$ and its modified nanocages.

$$E_{ads} = E_{(nanocage-APN)} - \left(E_{(nanocage)} + E_{(APN)}\right) + E_{BSSE} \quad (4)$$

Whereas, $E_{(nanocage\text{-}APN)}$ represents the energies of the complexes, $E_{nanocage}$ and E_{drug} denote the energies of the nanocages and drug, respectively, and E_{BSSE} stands for the energy of the basis set superposition error. The counterpoise (CP) approach, as described by Boys and Bernadi, was used to determine the adsorption energy, corrected for basis set superposition error (BSSE) [79].The thermodynamic parameters including enthalpy (ΔH), Gibbs free energy (ΔG), and entropy change (ΔS), for drug adsorption on nanocages at 298.15 K were calculated using Eqs. 2–4 [49].

The impact of water solvent on APN drug interactions with $B_{12}N_{12}$ and its Cu-modified $B_{12}N_{12}$ nanocages was examined using the self-consistent reaction field(SCRF) within the conductor-like polarizable continuum model (CPCM) [80]. Solvation energy (E_{solv}) was used to assess the complexes' solubility, through Eq. 5;

$$E_{solv} = E_{solvent} - E_{gas} \quad (5)$$

In this case, $E_{solvent}$ and E_{gas} stand for the solvent phase and gas phase energies, respectively.

The electronic charge transfer (Q_{CT}) was determined by investigating the variationin charge among the APN drug adsorbed on $B_{12}N_{12}$ or in Cu-modified $B_{12}N_{12}$ nanocages and the free APN drug, calculated using Eq. 6;

$$Q_{CT} = Q_{(nanocage-APN)} - Q_{APN} \quad (6)$$

Here $Q_{(nanocage\text{-}APN)}$ and $Q_{(APN)}$ denote the charges of APN drug adsorbed onto Cu-modified or $B_{12}N_{12}$ nanocages and free APN drug, correspondingly.

The electrophilicity index (ω) serves as a key parameter for quantifying the energy stabilization acquired by a system when receiving additional charge from the surrounding environment. Using eqs. 10–13 [63], global reactivity descriptors were assessed.

GaussSum, a potent technique, was utilized to produce the density of states (DOS) [81], providing comprehensive information about the orbital composition. This method facilitates the visualization of orbital distribution and composition, advancing the knowledge of electronic structures. QTAIM and non-covalent interaction (NCI) analyses were employed using **Multiwfn 3.7 [82]** to characterize the interaction between the Cu-modified nanocages and the drug. These approaches provide an in-depth investigation of the orbital composition, charge dissemination, and characteristics of the drug's and the nanocages' non-covalent interactions. We have also compared the delivery process and desorption mechanism at acidic pH levels due to the acidic nature of cancer cells [83]. The protonation model is utilized to examine the desorption of drugs from nanocages under acidic conditions, emphasizing the reversibility [84] of drug adsorption. All calculations, except those related to solvation effects, were conducted under gas phase conditions.

3. Results and discussion

3.1. Structural, stability, electronic and adsorption sites analysis

Fig. 1a illustrates the optimized $B_{12}N_{12}$ nanocage, computed using the B3LYP-GD3(BJ)/6-31G(d,p) basis set. The optimized $B_{12}N_{12}$ nanocage, which was computed applying the B3LYP-GD3(BJ)/6-31G(d,p) basis set, is shown in Fig. 1a. This nanocage has equal boron and nitrogen sites and is highly stable. It is made up of eight hexagonal rings and six tetragonal rings. In the $B_{12}N_{12}$ nanocage, the tetragonal rings' computed internal angles are B-N-B = 80.4° and N-B-*N* = 98.3° [85,86]. The nanocage exhibits two unique bond types: one connecting a hexagonal ring to tetragonal ring (b64) and another link two hexagonal rings (b66), measuring 1.484 Å and 1.436 Å, respectively, in the $B_{12}N_{12}$ structure. These values agree with previous theoretical studies and are consistent with experimental findings derived from mass spectroscopy analysis [31,87].

This research investigated varied sites for the Cu-modification on $B_{12}N_{12}$ nanocages, comprising of the configurations of different fashion like doped, decorated and encapsulation form. The designated positions were: (i) doped $CuB_{11}N_{12}$, (ii) doped $B_{12}N_{11}Cu$, (iii) b66(The Cu atom placed upon the bond linking to hexagonal rings), (iv) b64(where the Cu atom located upon the bond connecting the hexagonal and tetragonal ring), (v) B_{top}(The Cu atom on top of a boron atom), (vi) N_{top}(Cu on top of a nitrogen atom), (vii) r6 (Cu on top of the centre of a hexagonal ring), and (viii) r4(The Cu atom on top of the center of a tetragonal ring). After optimization, five stable structures were identified: doped configurations ($CuB_{11}N_{12}$ and $B_{12}N_{11}Cu$, involving the replacement of a boron or

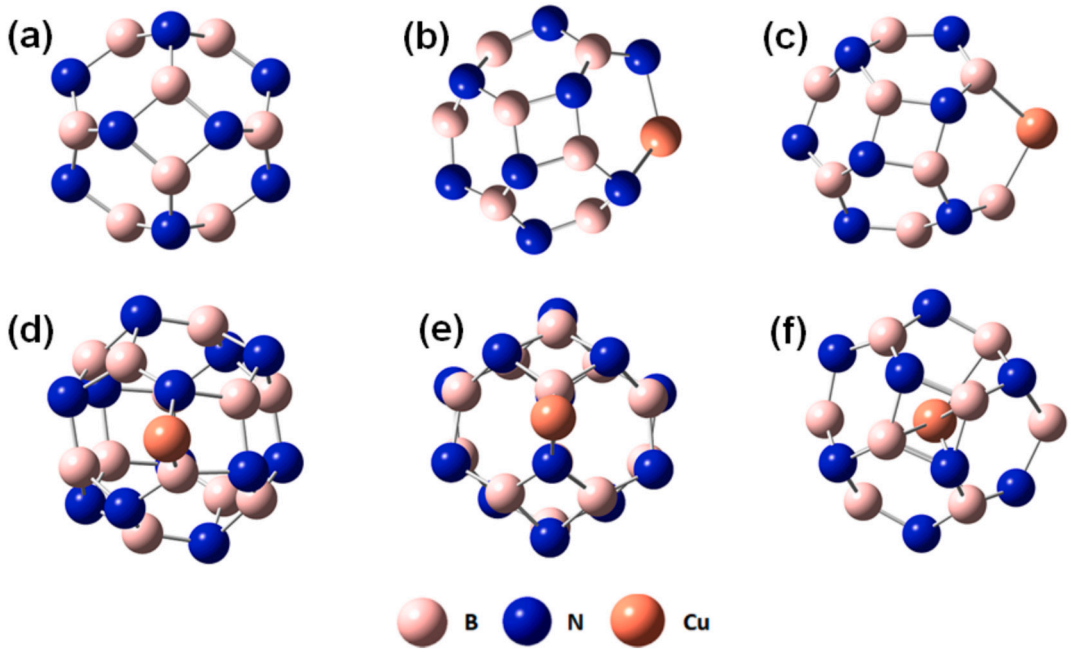

Fig. 1. Optimized structures for (a) isolated $B_{12}N_{12}$, (b) $CuB_{11}N_{12}$, (c) $B_{12}N_{11}Cu$, (d)Cu@b64(e) Cu@b66, and (f)Cu@$B_{12}N_{12}$ nanocages.

nitrogen atom with Cu), decorated nanocages (Cu@b64 and Cu@b66, where the Cu atom is upon the bond connection the hexagonal and tetragonal ring and upon the bond linking the two hexagonal rings as accordingly), and in case of encapsulated configuration (Cu@$B_{12}N_{12}$, where Cu resides inside the nanocage). Some initial geometries, such as Cu atop boron or nitrogen atoms, reshaped into these ultimate structures in the course of optimization. Fig. 1b and Fig. 1c represent the Cu-doped nanocages $CuB_{11}N_{12}$ and $B_{12}N_{11}Cu$, respectively.

Replacing boron or nitrogen atoms with Cu caused noticeable structural deformation in the $B_{12}N_{12}$ nanocage. Cu atoms protruded from the surface due to their greater atomic radius relative to boron and nitrogen. The effect is more noticeable in copper-doped systems like $B_{12}N_{11}Cu$, where the metal extends outward from the nanocage. Cu-modified $B_{12}N_{12}$ nanocage systems are typically assessed across multiple spin states to identify the most stable configuration. The partially filled d-orbitals of transition metals enable various electronic arrangements, resulting in multiple possible spin multiplicities. Spin-polarized calculations were employed to determine the ground-state spin state of the Cu-modified $B_{12}N_{12}$ nanocage, as summarized in Table S1.

In decorated nanocages, bond length variations and ring deformations are observed near the metal interaction site. In contrast, during geometry relaxation in the encapsulated system, the metal shifted away from the center of mass. Within the $CuB_{11}N_{12}$ nanocage, the longest and shortest Cu—N bond lengths were 1.887 Å and 1.859 Å, resultantly. This phenomenon was more evident in the $B_{12}N_{11}Cu$ nanocage. Within the $B_{12}N_{11}Cu$ nanocage, the maximum Cu—B bond distance extended to 2.006 Å, while the shortest was 1.927 Å. Two Cu-decorated optimized potential nanocages, designated as Cu@b64 and Cu@b66, respectively, are displayed in Fig. 1d and Fig. 1e. In the Cu@b66 nanocage, the maximum bond length of B—N extended to 1.545 Å, whereas in the Cu@b64 nanocage, the longest bond length reached 1.659 Å. The bond lengths of Cu@b66 and Cu@b64 nanocages show increases of 0.109 Å and 0.175 Å, respectively, compared to the pristine $B_{12}N_{12}$ nanocage. Fig. 1f illustrates the encapsulated Cu@$B_{12}N_{12}$ structure, where Cu is housed inside the nanocage, where the B—N bond lengths were b66 = 1.427 and b64 = 1.525, respectively. These bond lengths show slight deviations from those of pristine $B_{12}N_{12}$ [88,89].

In the present study, we employed the B3LYP functional with D3(BJ) dispersion correction and the 6-31G(d,p) basis set, which have been widely used for adsorption and interaction studies due to their good balance between accuracy and computational efficiency. However, we recognize that B3LYP may underestimate interaction energies in systems with transition metals due to complex exchange–correlation and d-orbital effects. We have also included results obtained using additional functionals, such as ωB97XD and M06-2×, to better evaluate the Cu interactions. This allowed us to assess the sensitivity of adsorption energies and electronic properties to the choice of exchange–correlation functional, ensuring the robustness of our findings. The data are included in Table S2.

As presented in Table 1, the optimized pristine $B_{12}N_{12}$ nanocage displayed a zero dipole moment and a band gap (E_g) of 6.87 eV, consistent with previous theoretical findings [87,90]. To find out the degree of metal interaction with the nanocages, the cohesion energy (E_{coh}) of Cu-modified systems was calculated. The cohesion energy of the isolated $B_{12}N_{12}$ nanocage is higher at −7.53 eV compared to its modified counterparts, indicating that modifications increase the reactivity of the nanocages. This behavior is widely reported in the literature [91]. In modified systems, copper placed outside the nanocage interacts more intensively with the structure. Consequently, systems with copper decoration show enhanced cohesion and increased stability compared to other modified nanocages. The values for the cohesive energy (E_{coh}) of the Cu-modified nanocages-$CuB_{11}N_{12}$, $B_{12}N_{11}Cu$, Cu@b64, Cu@b66 and Cu@$B_{12}N_{12}$ were − 7.36,-7.26,-7.38,-7.38, and − 7.19 eV, accordingly, relative to −7.53 eV for pristine $B_{12}N_{12}$, indicating higher stability for

Table 1
Calculated Values of Cohesive Energy (E_{coh}), Dipole Moment (μ_D), HOMO Energy (E_H), LUMO Energy (E_L), Band Gap (E_g) and Fermi Energy Level (E_F) for the Isolated Systems and Allopurinol (APN) Drug in gas phase.

System	E_{coh}(eV)	μ_D(Debye)	E_H(eV)	E_L(eV)	E_g(eV)	E_F(eV)
$B_{12}N_{12}$	−7.53	0	−7.72	−0.85	6.87	−4.29
$CuB_{11}N_{12}$	−7.36	1.71	−6.96	−5.01	1.95	−5.99
$B_{12}N_{11}Cu$	−7.26	2.07	−5.25	−2.48	2.77	−3.87
Cu@b64	−7.38	1.44	−4.86	−1.81	3.05	−3.34
Cu@b66	−7.38	1.69	−4.95	−1.60	3.35	−3.28
Cu@$B_{12}N_{12}$	−7.19	2.93	−3.75	−1.98	1.77	−2.87
APN	−6.51	3.64	−6.53	−1.11	5.42	−3.82

the pristine structure. The Cu-modified nanocages, despite having slightly less negative E_{coh} values, continue to be both viable and stable. Analogous patterns were noted in the metals Mn and Fe doping of $B_{12}N_{12}$ [28] as well as in the encapsulation of 3d, 4d, or 5d transition metals [89].

We have also investigated the thermal stability of Cu-modified $B_{12}N_{12}$ nanocages using ab initio molecular dynamics (AIMD) simulations conducted over 1000 fs at physiological temperature (310*K*). The AIMD analysis indicates that most systems remain stable, except for $CuB_{11}N_{12}$ and $B_{12}N_{11}Cu$, which exhibit slight deformation. Additionally, the 1000 fs simulation duration is considerable for conventional quantum MD, making it adequate to capture potential structural changes. The MD results for each system are presented in Fig. S1 in the supporting information.

The band gap of Cu-modified nanocages decreased significantly, spanning from 1.77 to 3.35 eV. Among these, $Cu@B_{12}N_{12}$ showed the most substantial change in E_g. Additionally, the modified nanocages' dipole moment increased, ranging from 1.44 to 3.93 D, with the highest increase observed in the $Cu@B_{12}N_{12}$ structure. These alterations indicate different types of interactions with the APN drug.

To investigate their efficacy as drug carriers, structural optimization of both pure and Cu-modified $B_{12}N_{12}$ nanocages was carried out using the APN drugs. Adsorption energy and molecular electrostatic potential (MEP) calculations identified active sites and interaction mechanisms. Various initial orientations of APN (vertical and horizontal) on the $B_{12}N_{12}$ nanocage were examined and are presented in Fig. S2. Based on the MEP of APN, its interaction with the $B_{12}N_{12}$ nanocage led to three stable configurations (A1, A2, and A3), as shown in Fig. 2. The adsorption energies, calculated using B3LYP-GD3(BJ), CAM-B3LYP, wB97XD, M06-2× and M08HX functionals, were − 33.50, −30.58, −33.70, −33.14 and − 32.60 kcal mol^{-1} for the most stable configuration(A2), respectively (Table S3). For the B3LYP-GD3(BJ) case, a minor deviation is observed from the A1 structure. The bond distance between the APN drug and the $B_{12}N_{12}$ nanocage, on the other hand, increases to 1.616 Å in the A3 configuration, decreasing the adsorption energy to −0.44 kcal mol^{-1}. Stronger adsorption was associated with the lesser distances, as observed in the configurationsA1 and A2. The variation in adsorption energies stems from the increased separation between the APN carbonyl group's oxygen atoms, the nitrogen atoms in the benzene and pentagon rings, and the $B_{12}N_{12}$ nanocage. MEP maps (as shown on Fig. 2) revealed negative regions on O and N atoms of APN, favoring interactions with the positively charged B atoms of $B_{12}N_{12}$. Similarly, negative MEP on the N atom of $B_{12}N_{12}$ made it susceptible to interaction with H atoms of APN. These observations were corroborated by average local ionization energy (ALIE) calculations, confirming the identified sites as more favorable for electrophilic attacks [92]. According to MEP map calculations and ALIE [92] evaluations from existing research, various initial arrangements of $B_{12}N_{12}$-APN complexes were developed taking into account electrostatic interactions, with the most energetically favorable configurations depicted in Fig. 2.

Fig. 3 shows the precise locations where the APN molecule adsorbs on the surface of the Cu-modified $B_{12}N_{12}$ nanocages, while the Table S4 outlines the changes in the bond lengths of the drug and nanocages before and after the interactions. While APN was being adsorbed on the pure $B_{12}N_{12}$ nanocage, a notable decline in bond length was observed; it went from 1.70 Å to 1.54 Å. Within the complex $CuB_{11}N_{12}$-APN, where the Cu_{24}-N_{36} bond length extended from 1.62 Å to 1.91 Å, the N_{21}-H_{37} bond slight expanded from 2.05 Å to 2.06 Å, and the N_{23}-H_{34} bond expanded from 2.69 Å to 2.96 Å. Similarly, for the $B_{12}N_{11}Cu$-APN complex, the Cu_{24}-N_{36} bond length extended to 1.95 Å from 1.82 Å.

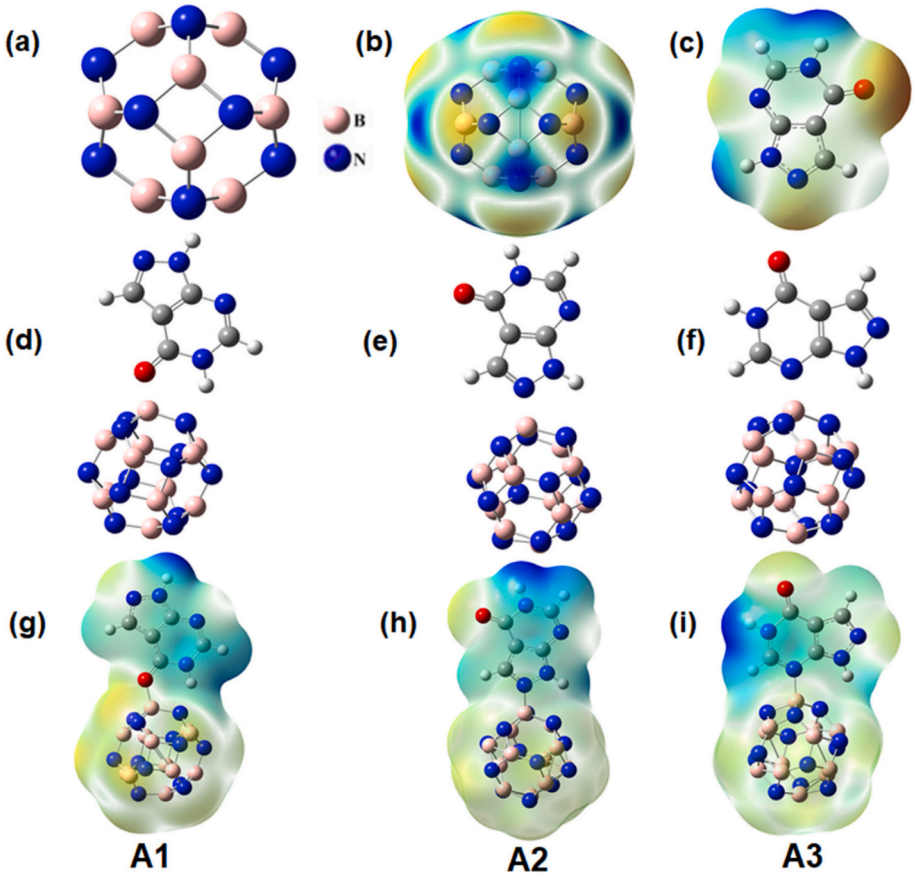

Fig. 2. Representations of optimized $B_{12}N_{12}$ (a), MFP of $B_{12}N_{12}$ (b), MEP of APN drug (c); optimized structures of A1(d), A2 (e), A3 (f); and MEPs of A1 (g), A2 (h) and A3 (I).

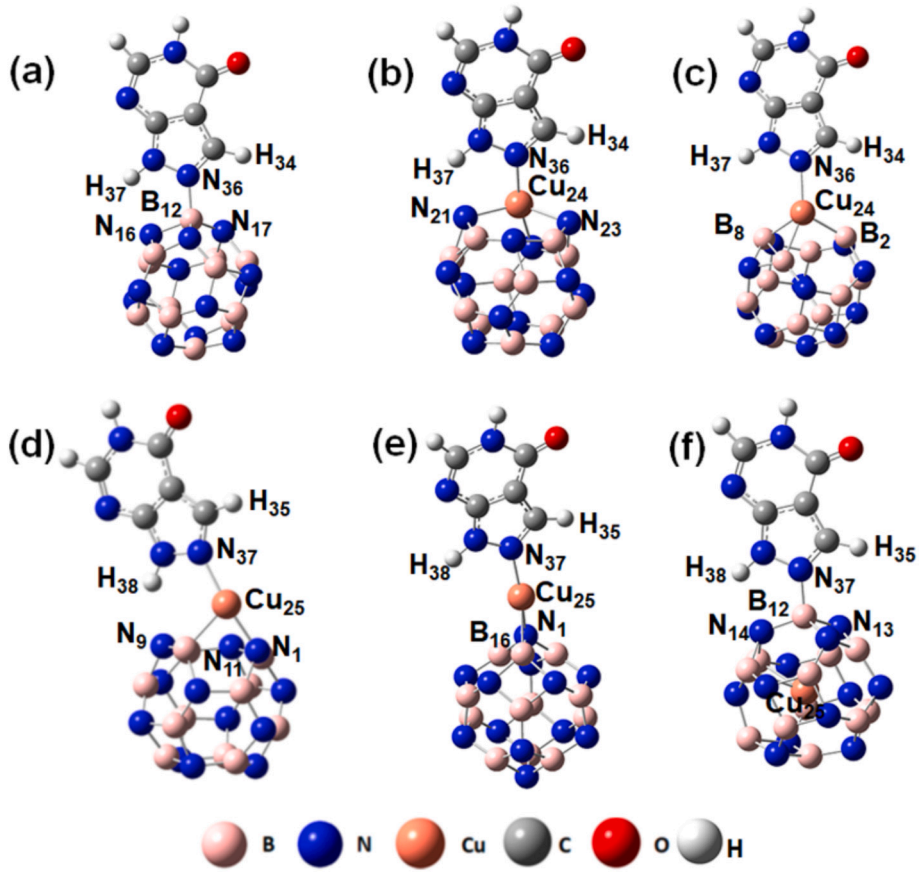

Fig. 3. Representations of the optimized geometries of (a) $B_{12}N_{12}$-APN (b) $CuB_{11}N_{12}$-APN, (c) $B_{12}N_{11}Cu$-APN, (d) Cu@b64-APN, (e) Cu@b66-APN, and (f) $Cu@B_{12}N_{12}$-APN.

Within the Cu@b64-APN complex the Cu_{25}-N_{37} bond length extended from 1.63 Å to 1.90 Å and in Cu@b66-APN complex decreases from 1.87 Å to 1.86 Å, accordingly. The $Cu@B_{12}N_{12}$-APN complex demonstrated a significant reduction in the length of the B_{12}-N_{37} bond, decreasing to 1.58 Å from 1.84 Å, a change of 0.26 Å. These modifications in the lengths of bonds signify structural expansion inside the complexes, indicative of increased reactivity following APN adsorption. The interacting complexes' optimized bond distances exhibited the pattern: $Cu@B_{12}N_{12}$-APN (1.58 Å) < Cu@b66-APN (1.86 Å) < Cu@b64-APN (1.90 Å) < $CuB_{11}N_{12}$-APN (1.91 Å) < $B_{12}N_{11}Cu$-APN (1.95 Å). This trend indicates that the Cu@b66-APN and the Cu@b64-APN complexes display moderate interaction lengths of approximately 1.86 Å and 1.90 Å, whereas the $CuB_{11}N_{12}$-APN and $B_{12}N_{11}Cu$-APN complexes display slightly extended bond lengths of interaction of 1.91 Å and 1.95 Å, correspondingly.

3.2. Adsorption of APN onto cu-modified $B_{12}N_{12}$ nanocages

The potential of $B_{12}N_{12}$ and its Cu-modified derivatives for APN drug delivery was evaluated through adsorption energy calculations using DFT at the B3LYP-GD3(BJ)/6-31G(d,p) level in gas and aqueous phases. The stable arrangements of APN bound to Cu-derived $B_{12}N_{12}$ nanocages are illustrated in Fig. 3 and Table 2 provides the calculated adsorption energies for various configurations ($CuB_{11}N_{12}$, $B_{12}N_{11}Cu$, Cu@b64, Cu@b66 and the $Cu@B_{12}N_{12}$). In this study, the adsorption performance of various Cu-modified nanocages with the APN drug was compared with previously reported results from the literature, as summarized in Table S5.

To ensure the validity of the adsorption energies in this study, we have also employed higher-level functionals such as M06-2× and ωB97XD. This comparative approach reinforces the consistency and reliability of the predicted adsorption trends across different computational methods. The corresponding adsorption energies are provided in Table S6. We have also evaluated the adsorption energies using a basis

Table 2
Calculated Bond Lengths (Å) after adsorption of APN, Adsorption Energy (E_{ads}), Enthalpy Change (ΔH), and Gibbs free energy (ΔG) in kcal mol^{-1} and change in entropy (ΔS) in kcal mol^{-1} K^{-1}, of all the Studied Complexes using the Optimized Structures in gas phase.

Systems	$d_{cage\text{-}N}$ (Å)	E_{ads} (kcalmol^{-1}) (B3LYP-GD(BJ))	ΔH (kcal mol^{-1})	ΔG (kcal mol^{-1})	ΔS (kcal mol^{-1} K^{-1}	E_{ads} (kcal mol^{-1}) (wB97XD)	ν_{max}(cm^{-1})	ν_{min} (cm^{-1})
$B_{12}N_{12}$-APN	1.595	−29.33	−32.01	−20.91	−0.040	−30.18	3465.71	25.12
$CuB_{11}N_{12}$-APN	1.905	−39.08	−46.88	−34.86	−0.040	−38.90	3467.16	20.09
$B_{12}N_{11}Cu$-APN	1.945	−25.50	−34.14	−23.47	−0.036	−25.34	3501.56	11.19
Cu@b64-APN	1.905	−29.97	−41.02	−29.15	−0.040	−28.74	3468.15	15.99
Cu@b66-APN	1.862	−22.11	−33.35	−23.27	−0.034	−24.50	3527.42	7.77
$Cu@B_{12}N_{12}$-APN	1.581	−35.74	−38.92	−26.39	−0.042	−36.34	3465.11	19.27

set with diffuse functions and compared them to those obtained without diffuse functions to assess their influence on the results. The adsorption energies decrease with diffuse functions because they better capture long-range, weak interactions like van der Waals(vdW) forces and reduce artificial over binding by accurately representing the delocalized electron density, leading to more realistic and typically lower adsorption energies. The corresponding data are provided in **Table S7**.

According to earlier research done by Mohsen Asle Zaeem et al. [93] and Tanveer Hussain et al. [94], adsorption energy values (E_{ads}) of about ±1 eV (±23 kcal mol^{-1}) are suggestive of either strong physisorption or weak chemisorption. In this study, the $B_{12}N_{11}$Cu-APN and Cu@b66-APN complexes exhibited strong physisorption, whereas the $CuB_{11}N_{12}$-APN, Cu@b64-APN and Cu@$B_{12}N_{12}$-APN complexes displayed chemisorption interactions. These findings suggest that Cu-modified $B_{12}N_{12}$ nanocages have a strong capacity to absorb the APN drug, highlighting their suitability for drug transport applications. The negative E_{ads} values for all complexes confirm the stable adsorption of APN in different orientations on Cu-functionalized $B_{12}N_{12}$ nanocages. The adsorption energies spanned from −34.10 to −49.30 kcal mol^{-1}, following the pattern $CuB_{11}N_{12}$-APN > Cu@b64-APN > Cu@$B_{12}N_{12}$-APN > $B_{12}N_{11}$Cu-APN > Cu@b66-APN. For APN adsorption onto pristine and Cu-modified $B_{12}N_{12}$ nanocages ($CuB_{11}N_{12}$-APN, $B_{12}N_{11}$Cu-APN, Cu@b64-APN, Cu@b66-APN, and Cu@$B_{12}N_{12}$-APN), the calculated E_{ads} values are −49.30, −35.55, −41.94, −34.10 and − 40.61 kcal mol^{-1}, consequently. The modified nanocages generally demonstrate enhanced drug adsorption in comparison to their pristine counterparts. The greatest adsorption energy was noted in the $CuB_{11}N_{12}$-APN complex (−39.08 kcal mol^{-1}), while the lowest was found in the Cu@b66-APN complex (−22.11 kcal mol^{-1}).

We agree that relativistic effects can influence Cu-modified $B_{12}N_{12}$ nanocage systems. We have also checked all the Cu-modified nanocages with effective core potentials (ECPs, e.g., LANL2DZ) to assess their impact on adsorption energetic. These tests confirmed that incorporating relativistic effects improves the reliability of Cu-centered interaction descriptions. The data are included in Table S8.

The counterpoise (CP) approach as outlined by Boys and Bernadi [79] was used to compute the BSSE-corrected adsorption energies. The BSSE values for Cu-modified $B_{12}N_{12}$-APN complexes, which range from 4.88 to 11.99 kcal mol^{-1}, are presented in Table S9. $CuB_{11}N_{12}$-APN, $B_{12}N_{11}$Cu-APN, Cu@b64-APN, Cu@b66-APN, and Cu@$B_{12}N_{12}$-APN complexes have BSSE values of 10.23, 10.05, 11.98, 11.99, and 4.88 kcal mol^{-1}, accordingly. The computed adsorption energies (E_{ads}) range from −22.11 to −39.08 kcal mol^{-1}, respectively, as shown in Table 2.

The incorporation of a Cu atom onto the $B_{12}N_{12}$ nanocages enhanced the adsorption process. Table 2 confirms the spontaneous adsorption of APN on Cu-modified $B_{12}N_{12}$ nanocages, indicated by the negative ΔG values and exothermic, as shown by the negative ΔH values. The E_{ads} values of the $CuB_{11}N_{12}$-APN, Cu@b64-APN, and Cu@$B_{12}N_{12}$-APN complexes were all greater than −27.21 kcal mol^{-1}, reflecting strong interactions that may reduce their suitability for sensor applications, unlike the Cu@b66 nanocage. The Cu@b66 and $B_{12}N_{11}$Cu nanocage complex exhibited an E_{ads} value of −22.11 and − 25.50 kcal mol^{-1}, falling within the range of −8.16 to-27.21 kcal mol^{-1} [95], indicative of moderate interactions with the APN. Among these, it suggests that Cu@b66 nanocage is the most suitable as a drug carrier, as it interacts with the APN via a robust physisorption or mild chemisorption process, it ensures efficient adsorption-desorption dynamics with optimal recovery times.

The complexes' deformation energies, presented in Table S9, were positive, indicating structural distortions from their relaxed states upon adsorption. The investigation of the APN drug's electronic configuration after adsorption revealed a band gap (E_g) of 5.37 eV, where the HOMO at −6.42 eV and the LUMO -1.05 eV. Before adsorption, the HOMO and LUMO were − 6.53 eV and − 1.11 eV, respectively, with an E_g of 5.42 eV. These findings show minimal alteration within the APN electronic configuration followed the nanocages' adsorption, indicating that the process of adsorption has a negligible effect on the drug's electronic characteristics.

To investigate adsorption of the drug on the nanocage surfaces, the adsorption enthalpy (ΔH), Gibb's free energy (ΔG) of the complexes were calculated under the standard conditions(1 atm and 298.15 K). The calculated negative ΔH and ΔG values validated that the adsorption process is both exothermic and spontaneous. The order of negative ΔG values, Cu@b66-APN < $B_{12}N_{11}$Cu-APN < Cu@$B_{12}N_{12}$-APN < Cu@b64-APN < $CuB_{11}N_{12}$-APN, demonstrated the progressive spontaneity of interaction between the APN drug and with the Cu-modified $B_{12}N_{12}$ nanocages. Furthermore, the study assessed these nanocages' potential as efficient drug carriers.

3.3. Electronic properties

Investigating electron densities and energy states offers valuable insights into the influence of Cu modification and APN adsorption on $B_{12}N_{12}$ and its Cu-modified $B_{12}N_{12}$ nanocages. Fig. 4 illustrates the different optimized geometries of APN adsorbed onto Cu-modified $B_{12}N_{12}$ nanocages. Table 3 presents key orbital parameters, such as the HOMO and LUMO energies, the Fermi level energies (E_F) and the energy gap (E_g). The pristine $B_{12}N_{12}$ exhibits semiconductor properties with the energy gap (E_g) of 6.87 eV, with HOMO-LUMO energies of −7.72 eV and − 0.86 eV, respectively, and the Fermi level at −4.29 eV.

Upon Cu incorporation, the HOMO-LUMO energies change [96]. Within the $CuB_{11}N_{12}$ nanocage, HOMO energy increases to −6.96 eV, while the LUMO energy drops to −5.01 eV, resulting in a narrower energy gap (E_g) of 1.95 eV, while the Fermi level energy shifts to −5.99 eV. In the case of the $B_{12}N_{11}$Cu nanocage, the HOMO energy rises to −5.25 eV, while the LUMO energy reduces to −2.48 eV, yielding a narrowed HOMO-LUMO energy gap of 2.77 eV, and the Fermi level located at −3.87 eV. The noted variations results from the stabilization of LUMO and the destabilization of HOMO orbital. In case of the nanocages Cu@b64 and Cu@b66, energies of the HOMO increase to −4.86 eV and − 4.95 eV, respectively, and the LUMO energies decrease to −1.81 eV and − 1.60 eV, resulting in the energy gap of 3.05 eV and 3.35 eV, with the Fermi level energies at −3.34 eV and − 3.28 eV. On the other hand, the energies of HOMO-LUMO of the Cu@$B_{12}N_{12}$ nanocage are −3.75 eV and − 1.98 eV, respectively, with the energy gap at 1.77 eV and the Fermi level at −2.87 eV respectively.

The electronic properties of drug and Cu-modified $B_{12}N_{12}$ nanocages were analyzed, with HOMO, LUMO and the FMOs depicted in Fig. 4. Significant changes in the HOMO and LUMO energy levels were noticed as a result of drug adsorption on the nanocages. The reduction in HOMO energy lowered ionization energy, facilitating electron flow upon APN adsorption. At first, the orbitals HOMO and LUMO were evenly spread throughout the drug. The distribution of orbitals became uneven after drug adsorption, resulting from the charge transfer between the drug and the nanocages. After adsorption of drug on nanocages, the HOMO remained unchanged, keeping uniform distribution across the molecule, whereas the LUMO mostly concentrated on the APN molecule, with a portion delocalized amidst nanocages and drug. The observed overlap between APN drug and the nanocages indicates strong chemical bonding and interactions. FMO analysis revealed there activity of the metal-doped nanocages, providing insights into the calculation of electron affinity ($A = -E_{LUMO}$) and the ionization potential ($I = -E_{HOMO}$). The complex's reactivity increased due to the reduced HOMO energy, which lowered the ionization potential. Conversely, the increase in LUMO energy raised the electron affinity, suggesting heightened reactivity, particularly in the Cu@b66-APN complex. Cu incorporation in the $B_{12}N_{12}$ nanocages, pushed the HOMO toward the Cu via nanocages, increasing its electron density. However, because of its electropositive nature, the metal couldn't keep the extra electrons, causing their redistribution.

The HOMO-LUMO gap (E_g) correlates with conductivity through the interaction of higher HOMO energy levels [97]. The results obtained

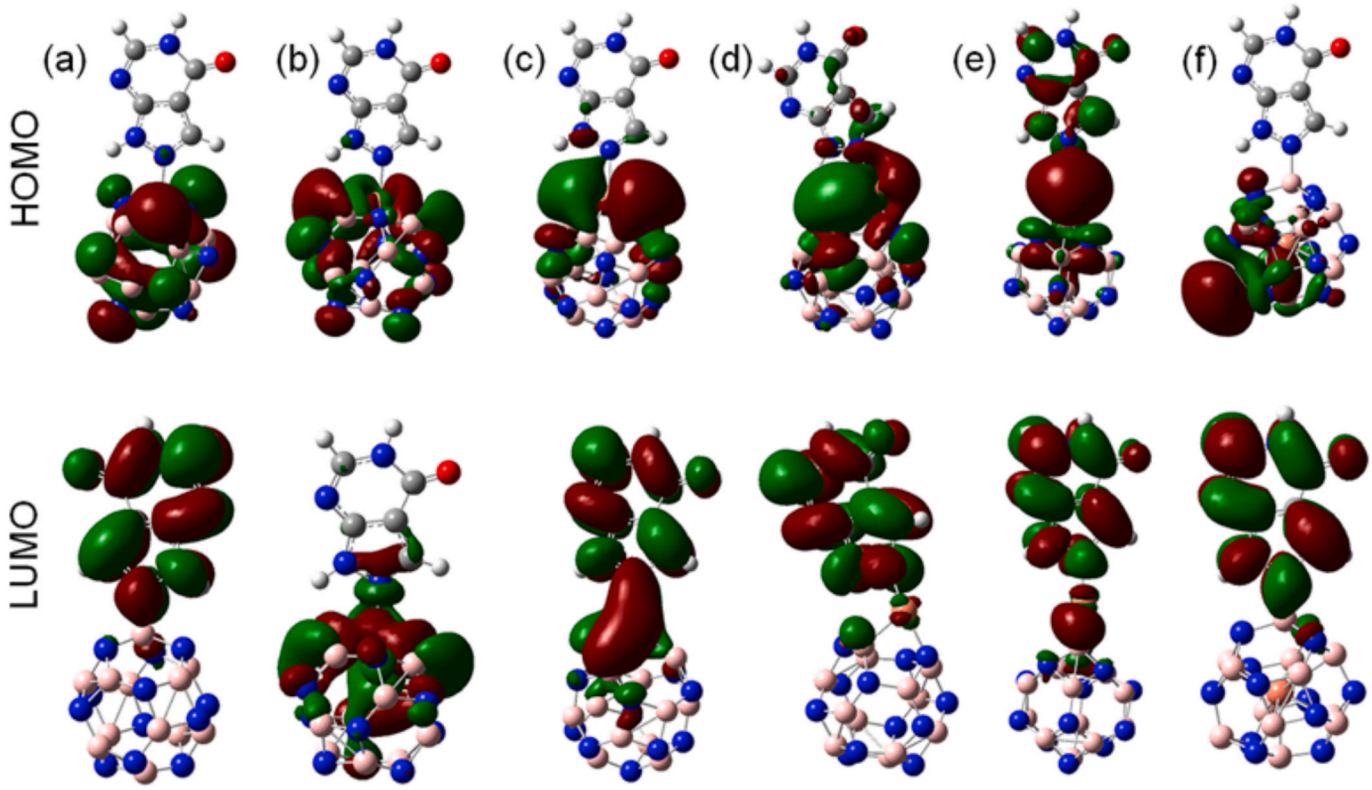

Fig. 4. Three–dimensional maps of the HOMO-LUMO electron distribution of the complexes (a) $B_{12}N_{12}$-F (b) $CuB_{11}N_{12}$-APN, (c) $B_{12}N_{11}Cu$-APN, (d) Cu@b64-APN, (e) Cu@b66-APN, and (f) Cu@$B_{12}N_{12}$-APN.

Table 3
Calculated Values of Dipole Moment (Debye), HOMO Energy (E_H), LUMO Energy (E_L), Energy Gap (E_g), Electronic Sensitivity (% ΔE_g), Fermi Energy Level (E_F) and the fractional charge transfer Q_{CT} (Q_{CT} for the complexes between APN drug and Isolated Nanocages) in gas phase.

system	DM(Debye)	E_H	E_L	E_g	%ΔE_g	E_F	Q_{CT}
$B_{12}N_{12}$-APN	10.36	−6.77	−2.39	4.38	36.24	−4.58	−0.346
$CuB_{11}N_{12}$-APN	8.39	−6.60	−3.98	2.62	34.36	−5.29	−0.207
$B_{12}N_{11}Cu$-APN	8.85	−4.65	−2.17	2.48	10.47	−3.41	−0.166
Cu@b64-APN	7.89	−4.29	−2.01	2.28	25.25	−3.15	−0.085
Cu@b66-APN	8.70	−3.60	−2.20	1.40	58.21	−2.90	0.039
Cu@$B_{12}N_{12}$-APN	12.36	−3.40	−2.39	1.01	42.94	−2.90	−0.348
APN	3.64	−6.53	−1.11	5.42	–	−3.82	–

from this study reveal a reduction in LUMO energies for the modified nanocage structures compared to the $B_{12}N_{12}$ nanocage. The binding of the APN on Cu-modified $B_{12}N_{12}$ nanocages resulted in notable stabilization of both HOMO and LUMO energy levels. The Fermi level energies of the complexes $CuB_{11}N_{12}$-APN, $B_{12}N_{11}Cu$-APN, Cu@b64-APN, Cu@b66-APN, and Cu@$B_{12}N_{12}$-APN were calculated as −5.99 eV, −3.87 eV, −3.34 eV, −3.28 eV, and − 2.87 eV, respectively. APN adsorption on Cu diminished the Cu-$B_{12}N_{12}$ interaction, leading to reduced electron repulsion at the metal center due to decreased coordination. In the APN-Cu@$B_{12}N_{12}$ system, the HOMO displayed a dense concentration on the metal, with a more spread-out distribution across the nanocage. Additionally, APN adsorption caused a reduction in LUMO energy levels, signifying a movement toward the nanocage and boosting its stability via lower energy states.

The conductivity (σ) of $B_{12}N_{12}$ and its Cu-modified variants interacting with the APN was calculated using Eq. 8;

$$\sigma = AT^{3/2}e^{-E_g/2K_BT} \tag{8}$$

Here, σ represents the conductivity, E_g denotes the gap of energy between the HOMO and LUMO, K_B for the Boltzmann constant and T refers to the temperature. Eq. 8 indicates that a decrease in the energy gap (E_g) leads to a notable enhancement in electrical conductivity. This study reveals substantial improvements in both conductivity and sensing performance for APN adsorption in Cu-modifiedCu@b66 nanocages, surpassing the pristine $B_{12}N_{12}$ and the other modified nanocages.

As presented the data in Table 3, the charge transfers (Q_{CT}) is a crucial parameter for assessing the charge transfer during adsorption. A Q_{CT} value less than zero signifies charge transfer from drug to the carrier, whereas a value greater than zero indicates sift of charge from the carrier o drug. In the analyzed complexes, all calculated Q_{CT} values exhibited negative signs, suggesting that the charge was transferred from the drug to the nanocages [73]. The computed charge amounts that were transferred were − 0.207 e, −0.166 e, −0.085 e − 0.039 e and − 0.348 e for $CuB_{11}N_{12}$-APN, $B_{12}N_{11}Cu$-APN, Cu@b64-APN, Cu@b66-APN and Cu@$B_{12}N_{12}$-APN complexes, respectively. The negative Q_{CT} values noted in the Cu-modified nanocage systems confirm the stability of the complexes after their interaction with the drug, further supporting their role as effective nanocarriers.

3.4. Dipole moment analysis

The dipole moment of APN drug, shown in Table 3 before adsorption

is 3.64 Debye, demonstrating its polarity. The dipole moments were evaluated for the $B_{12}N_{12}$, Cu-modified $B_{12}N_{12}$ nanocages and Cu-modified $B_{12}N_{12}$-APN complexes to investigate their electrostatic characteristics. The pure $B_{12}N_{12}$ nanocage has a zero dipole moment due to its symmetrical structure. However, when Cu is introduced on the $B_{12}N_{12}$ nanocage, the dipole moment increases from 2.05 to 3.17 D. This change in dipole moment arises from the Cu atom, which alters the charge distribution and disrupts the charge separation within the $B_{12}N_{12}$ nanocages. The $B_{12}N_{11}Cu$ and $Cu@B_{12}N_{12}$ systems exhibit higher DM values, 2.07 and 2.93 D, suggesting reduced charge distribution within the nanocage. The dipole moments for APN-adsorbed Cu-modified $B_{12}N_{12}$ complexes range from 7.89 to 12.36 D. APN adsorption on Cu-modified $B_{12}N_{12}$ nanocages shifts the dipole moment because the drugs and nanocages transfer charges. As a result, the complex's dipole

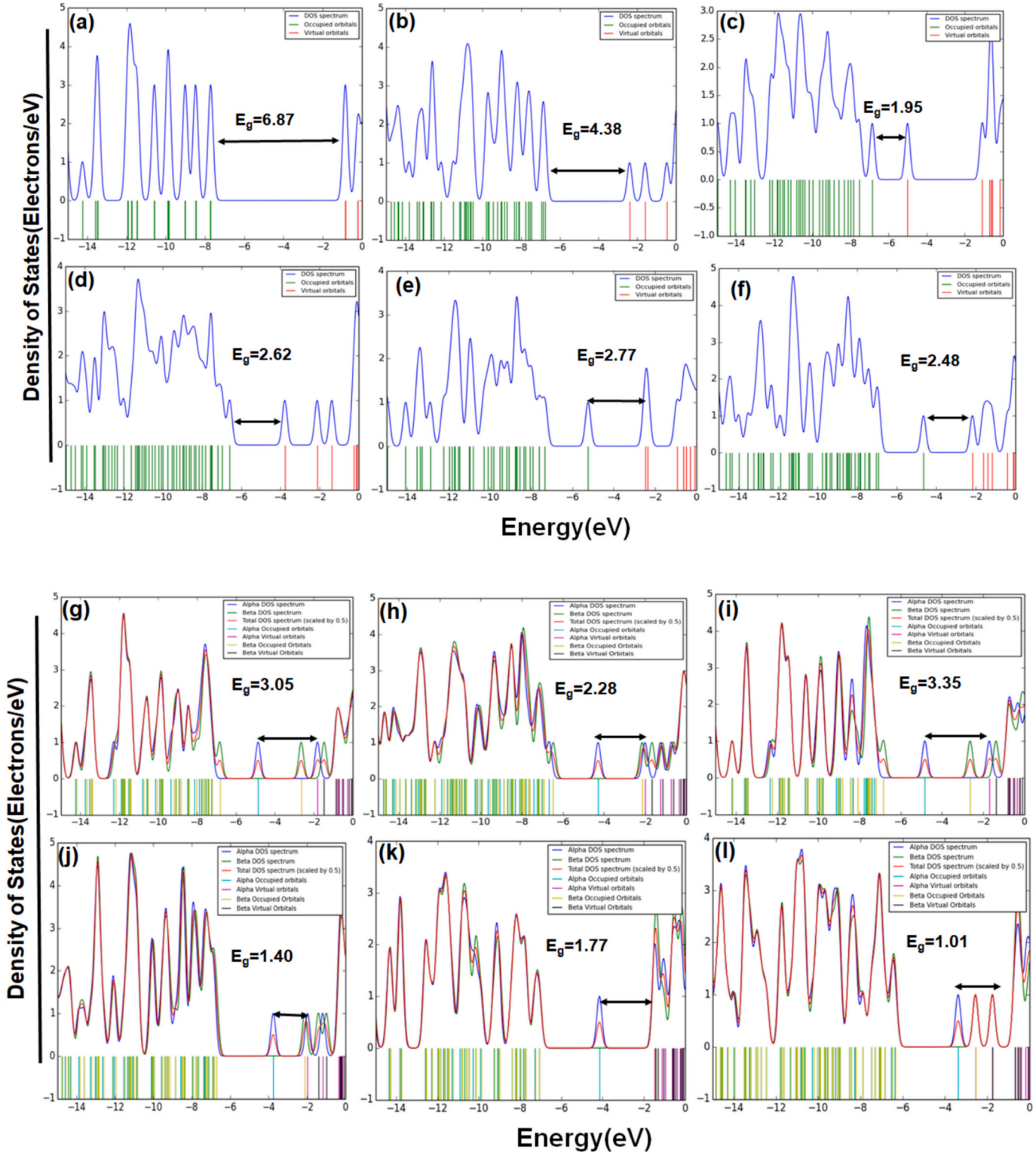

Fig. 5. Density of States (DOS) diagrams of isolated (a) $B_{12}N_{12}$, (b) $B_{12}N_{12}$-APN, (c) $CuB_{11}N_{12}$, (d) $CuB_{11}N_{12}$-APN, (e) $B_{12}N_{11}Cu$, (f) $B_{12}N_{11}Cu$-APN, (g) Cu@b64, (h) Cu@b64-APN, (i) Cu@b66, (j) Cu@b66-APN, (k) $Cu@B_{12}N_{12}$ and (l) $Cu@B_{12}N_{12}$-APN.

moment increases, improving drug delivery in the body. The greatest dipole moment increase occurs when APN is adsorbed onto the Cu@$B_{12}N_{12}$ nanocage (12.36 D), while the Cu@b64-APN complex exhibits the lowest change in dipole moment (7.89 D). Cu doping significantly boosts the dipole moments of both the complex and the drug it contains. The trend of dipole moment of the complexes is as follows: Cu@$B_{12}N_{12}$-APN > $B_{12}N_{11}$Cu-APN > Cu@b66-APN > Cu@b64-APN > $CuB_{11}N_{12}$-APN.

3.5. Density of states (DOS)

The density of states (DOS) analysis, illustrated in Fig. 5, highlights how the APN drug interacts with the Cu-modified $B_{12}N_{12}$ nanocages. This examination clearly emphasizes the variations in energy gap (E_g) induced by the adsorption of the APN drug onto different Cu-modified $B_{12}N_{12}$ nanocages. The DOS analysis evaluates the distribution of the electron states across various energy levels, where smaller values signify limited accessible states, whereas higher values denote a greater availability of states. The DOS analysis in Fig. 5 shows that APN adsorption on Cu-modified $B_{12}N_{12}$ nanocages reduces E_g, suggesting a shift to semiconductor behavior. The energy gap is important because it reflects the energy required to excite outer shell electrons into charge carriers, a key factor for determining electrical conductivity. The analysis of the DOS revealed that the drug molecules primarily affected the HOMO energy level, while enhanced LUMO activity in Cu-modified $B_{12}N_{12}$ nanocages drove the adsorption mechanism. The LUMO orbital distribution reflects APN's significant role in forming the TDOS of the complexes. The energy of LUMO of the Cu-modified $B_{12}N_{12}$ nanocages underscores their key role in adsorption, showcasing strong potential as electrochemical sensors. The bonding features within the DOS were observed between 4.0 and − 16 eV. The calculated Fermi energy levels for the Cu-modified complexes were − 5.29 eV, −3.41 eV, −3.15 eV, −2.90 eV, and − 2.90 eV for $CuB_{11}N_{12}$-APN, $B_{12}N_{11}$Cu-APN, Cu@b64-APN, Cu@b66-APN, and Cu@$B_{12}N_{12}$-APN, accordingly. Important information about the adsorption kinetics and chemical properties of the Cu-modified $B_{12}N_{12}$ nanocages binding with the APN drug is provided by the DOS analysis.

3.6. Global reactivity descriptors

Global reactivity descriptors (*IP, EA, μ, η, ω, S*) were computed to investigate the complexes' stability and reactivity via the B3LYP-GD3 (BJ)/6-31G(d,p), as summarized in Table 4, offering key insights into their nature. The global reactivity descriptors include global softness (*S*), global hardness (η), electrophilicity index (ω), chemical potential (μ), ionization potential (*IP*), and electron affinity (*EA*).

Chemical softness and hardness are crucial for understanding molecular reactivity and stability. Hard species are less polarizable, more stable, and tend to form strong interactions with other hard species, while soft species are more polarizable and reactive; preferring to interact with other soft species. The chemical hardness (η) is a measure of resistance to charge transfer. Softer systems (lower η) are more polarizable and can interact more flexibly with adsorbates, often correlating with better adsorption or release dynamics. The calculated chemical hardness data indicate that $B_{12}N_{12}$ ($\eta = 3.44$ eV) is the hardest cage species. Among the modified nanocages, Cu@b66 exhibits the highest hardness ($\eta = 1.68$ eV), while Cu@$B_{12}N_{12}$ shows the lowest ($\eta =$ 0.89 eV). In contrast, higher global softness (*S*) enhances responsiveness but reduces stability. Chemical potential (μ) gives insight into the system's ability to donate electrons. It helps predict electron flow between the cage and the drug molecule. Increased level of chemical potential (μ) indicates increased reactivity and reduced chemical stability. **Electrophilicity Index (ω)** quantifies the tendency of the nanomaterials to accept electrons. A higher ω can indicate a stronger ability to interact with electron-rich drugs (like APN), impacting adsorption strength and stability. According to the principles of maximum hardness (η) [98] and minimum electrophilicity (ω) [99] proposed by Parr and Pearson, systems exhibiting higher chemical hardness and lower electrophilicity exhibit greater stability.

Before APN adsorption, the global hardness (η) values were 0.98, 1.39, 1.53, 1.68, and 0.89 for Cu-modified $CuB_{11}N_{12}$, $B_{12}N_{11}$Cu, Cu@b64, Cu@b66, and Cu@$B_{12}N_{12}$ nanocages, respectively. After APN adsorption, these values shifted to 1.31, 1.24, 1.14, 0.70, and 0.51 eV, indicating their enhanced reactivity and robustness. The global softness values varied with a range of 0.30 to 0.56 eV for the modified nanocages and from 0.38 to 0.89 eV for the complexes. The chemical potential (μ) values for the complexes were ranked as follows: $CuB_{11}N_{12}$-APN > $B_{12}N_{11}$Cu-APN > Cu@b64-APN > Cu@b66-APN > Cu@$B_{12}N_{12}$-APN, with values of −3.96, −2.95, −2.72, −2.15, and − 1.77 eV, respectively. Strong electrophilic properties were observed in $CuB_{11}N_{12}$-APN (5.97 eV), $B_{12}N_{11}$Cu-APN (3.50 eV), and Cu@b66-APN (3.30 eV). Cu-modification of $B_{12}N_{12}$ improved the electrophilicity index, albeit with a minor decrease in the Cu-decorated and encapsulated nanocage systems. The computed adsorption energy, derived from these descriptors, prioritized the ranking of the complexes as follows: $CuB_{11}N_{12}$-APN > Cu@b64-APN > Cu@ $B_{12}N_{12}$-APN > $B_{12}N_{11}$Cu-APN > Cu@b66-APN showing their tremendous sensitivity and reaction. **Electronegativity (χ)** reflects the tendency of the nanocage to attract electrons. Systems with high electronegativity are more likely to accept electrons from adsorbed drug molecules, influencing adsorption strength. The reduced electronegativity of APN drug relative to the Cu-modified $B_{12}N_{12}$ nanocages suggests electron transfer from the APN drug to the nanocages. This electron transfer, where the APN as the donor and nanocages serve as the acceptor, is confirmed by the negative charge transfer (Q_{CT}) values, which indicate that electrons flow from the drug APN to the $B_{12}N_{12}$ nanocages.

Table 4
The Energy gap (E_g), Ionization Potential(*IP*), Electron Affinity(*EA*), Chemical Potential(μ), Electrophilic Index(ω), Chemical Hardness(η), Chemical Softness(*S*) and Electronegativity(χ) calculated for all systems. All units are electron volt (eV) calculated at B3LYP-GD3(BJ)/6-31G(d,p) basis set in gas phase.

Systems	E_g	*IP*	*EA*	μ	ω	η	*S*	χ
APN	5.42	6.53	1.11	−4.62	3.94	2.71	0.18	4.62
$B_{12}N_{12}$	6.87	7.72	0.85	−5.58	4.53	3.44	0.15	5.58
$CuB_{11}N_{12}$	1.95	6.96	5.01	−3.97	8.07	0.98	0.51	3.97
$B_{12}N_{11}$Cu	2.77	5.25	2.48	−3.32	3.97	1.39	0.36	3.32
Cu@b64	3.05	4.86	1.81	−3.19	3.34	1.53	0.33	3.19
Cu@b66	3.35	4.95	1.60	−3.31	3.28	1.68	0.30	3.31
Cu@$B_{12}N_{12}$	1.77	3.75	1.98	−2.32	3.03	0.89	0.56	2.32
$B_{12}N_{12}$-APN	4.38	6.77	2.39	−4.48	4.58	2.19	0.23	4.48
$CuB_{11}N_{12}$-APN	2.62	6.60	3.98	−3.96	5.97	1.31	0.38	3.96
$B_{12}N_{11}$Cu-APN	2.48	4.65	2.17	−2.95	3.50	1.24	0.40	2.95
Cu@b64-APN	2.28	4.29	2.01	−2.72	3.23	1.14	0.44	2.72
Cu@b66-APN	1.40	3.60	2.20	−2.15	3.30	0.70	0.71	2.15
Cu@$B_{12}N_{12}$-APN	1.01	3.40	2.39	−1.77	3.03	0.51	0.99	1.77

3.7. NBO analysis

Natural Bond Orbital (NBO) analysis serves as an effective method for exploring both intra- and intermolecular interactions, hybridization states, and charge transfer dynamics between nanocages and the drug. This technique was employed to transform from atomic orbitals (AOs) to natural bond orbitals (NBOs). It promotes the movement of electron density from donor to acceptor NBOs, enhancing the overall delocalization process, converting delocalized into localized molecular orbitals, and highlighting key aspects of chemical bonding. The second-order perturbation energy (E^2) for the donor(i)-acceptor (j) interactions, including $n \rightarrow \sigma^*$ or $\sigma \rightarrow \sigma^*$ charge transfer, was calculated to assess both intermolecular and intramolecular charge transfer. Forward electron excitations were observed in all Cu-modified interactions.

The highest E^2 values, ranging from 13.65 to 70.77 kcal mol^{-1}, are observed during the interaction of APN with Cu-modified nanocages, primarily due to charge movement from APN's nitrogen lone pair to Cu antibonding orbital. For the $CuB_{11}N_{12}$-APN complex, the E^2 value for the $n(N_{36(APN)}) \rightarrow \sigma^*(Cu_{24})$ interaction is 59.14 kcal mol^{-1}. For $B_{12}N_{11}$Cu-APN, the E^2 value is 70.77 kcal mol^{-1} for the transition, $n(N_{36(APN)}) \rightarrow \sigma^*(Cu_{24})$. For the Cu@b64-APN complex, the highest E^2 value is 21.63 kcal mol^{-1} for the $n(N_{37(APN)}) \rightarrow n^*(Cu_{25})$ interaction, while for the Cu@b66-APN complex, the stabilization energy for the $n(N_{37(APN)}) \rightarrow n^*(Cu_{25})$ transition is 13.65 kcal mol^{-1}. In the Cu@$B_{12}N_{12}$-APN complex, the transfer of charge happens for $\sigma \rightarrow \sigma^*$ transition, with the E^2 values making bond between APN's nitrogen and boron of nanocage being 2.25, 2.26 and 1.16 kcal mol^{-1} for $\sigma(C_{39}\text{-}N_{37(APN)}) \rightarrow \sigma^*(B_{12}\text{-}N_{37(nanocage)})$, $\sigma(B_{12}\text{-}N_{37(nanocage)}) \rightarrow \sigma^*(N_{37}\text{-}C_{39(APN)})$, $\sigma(B_{12}\text{-}N_{14(nanocage)}) \rightarrow \sigma^*(N_{37}\text{-}C_{39(APN)})$, correspondingly. When APN adsorbed on pristine $B_{12}N_{12}$, the transfer of charge occurs for the transition $\sigma(B_{10}\text{-}N_{13(nanocage)}) \rightarrow \sigma^*(B_{12(nanocage)}\text{-}N_{35(APN)})$ and $\sigma(C_{37}\text{-}N_{35(APN)}) \rightarrow \sigma^*(B_{12(nanocage)}\text{-}N_{35(APN)})$ with E^2 values of 13.70 and 4.32 kcal mol^{-1}, respectively. The second-order perturbation energies (stabilization energy) between the filled and empty orbitals, which highlight significant charge transfer within the intermolecular NBOs, are summarized in Table S10.

3.8. Sensor mechanism

Identifying key sensing parameters is essential for assessing the performance of nanocages in sensing applications. The work function (Φ) is crucial as it represents the energy needed to move an electron from the Fermi level to the vacuum level.

This parameters has been emphasized by researchers such as Mollania et al. [100], Mirhaji et al. [101], and Cachaneski-Lopes and Batagin-Neto et al. [102] for its critical role in material characterization. The Fermi energy provides valuable insights into the interaction between doped -$B_{12}N_{12}$ nanocages and the APN drug. The electrical behavior of a sensor material is determined the energy gap between its highest and lowest molecular orbitals (E_g) and its work function (Φ). A smaller E_g indicates improved electron transport efficiency among the conduction band and the valence bands. The work function (Φ) is calculated applying the Eq. 9;

$$\Phi = V_{el(+\infty)} - E_F \tag{9}$$

Here, $V_{(el(+\infty))}$ denotes the electrostatic potential energy in vacuum (supposed to be approximately 0), and E_F denotes the Fermi level energy. By setting $V_{el(+\infty)} = 0$, the work function Φ can be expressed as $\Phi = -E_F$, according to Eq. 9. Therefore, the work function and Fermi level energy are directly related, as demonstrated in Table 5.

Dushman [103] in his study, demonstrated that deviations in the work function (Φ) can lead to changes in current densities, as measured by the Kelvin prove method. The change in emission properties in presence of an electric field produces electrical signals, enabling the identification and detection of particular chemical compounds. The

Table 5
Values of Electronic Sensitivity (% ΔE_g), Fermi Level Energy (E_F), Work Function (Φ), Changes in Work Function (% $\Delta\Phi$) and calculated NBO charges on Cu on the nanocages calculated using B3LYP-GD3(BJ)/6-31G(d,p) basis set in gas phase.

systems	% ΔE_g	E_F(eV)	Φ(eV)	% $\Delta\Phi$	$Q(e)$ on Cu
APN		−3.82	3.82		
$B_{12}N_{12}$		−4.29	4.29		
$CuB_{11}N_{12}$		−5.99	5.99		1.116
$B_{12}N_{11}Cu$		−3.87	3.87		0.647
Cu@b64		−3.34	3.34		0.536
Cu@b66		−3.28	3.28		0.514
Cu@$B_{12}N_{12}$		−2.87	2.87		0.581
$B_{12}N_{12}$-APN	36.24	−4.58	4.58	6.76	
$CuB_{11}N_{12}$-APN	34.36	−5.29	5.29	12.63	1.073
$B_{12}N_{11}$Cu-APN	10.47	−3.41	3.41	11.89	0.453
Cu@b64-APN	25.25	−3.15	3.15	5.69	0.830
Cu@b66-APN	58.21	−2.90	2.90	12.23	0.780
Cu@$B_{12}N_{12}$-APN	42.94	−2.90	2.90	5.32	0.596

Richardson-Dushman equation provides a clear relationship between work function and emitted electron density(j) from the solid surface, which is given by the following Eq. 10:

$$j = AT^2 e^{-\Phi/K_B T} \tag{10}$$

Here A is the Richardson constant (A/m^2), T stands for temperature, Φ is the work function, and K_B is the Boltzmann constant and j signify current density. This equation highlights the dependence of electron emission on the work function, temperature, and the properties of the material.

The values of work function of isolated Cu-modified nanocages, ranging from 2.87 to 5.99 eV, are presented in Table 5. These values decrease to a range of 2.90 to 5.29 eV after drug adsorption. This decline in work function suggests an electron transfer from the APN drug to the modified nanocages, followed by the flow of electrons into the adsorbed complexes. After adsorption, the energy gap reduces due to charge transfer. The modified nanocages demonstrate changeable degrees of change upon interacting with APN, with percentage variations of 58.21 %, 42.94 %, 34.36 %, 25.25 %, 10.47 % and observed for Cu@b66-APN, Cu@$B_{12}N_{12}$-APN, $CuB_{11}N_{12}$-APN, Cu@b64-APN, and $B_{12}N_{11}$Cu-APN accordingly. With significant percentage changes and decreased energy gap values, these nanocages demonstrate strong potential as efficient work function sensors for the detection of drug. Among the nanocages, the decorated Cu@b66 nanocage system demonstrated the highest sensitivity (ΔE_g = 58.21 %) for the APN drug. The fraction of electron transfer calculation evaluates the electron affinity of the surface and drug, while also examining the chemical stability of these systems. This calculation provides crucial information about the electron flow from the drug (adsorbate) to the adsorbent nanocage surfaces, elucidating potential of their charge interaction.

3.9. QTAIM investigation

The analysis of bond critical points (BCPs) offers valuable insight into the nature and strength of intermolecular interactions at the electronic level, as described within the framework of quantum theory of atoms in molecules (QTAIM) developed by Bader and collaborators. The Multiwfn program suite [82] is employed to analyze topological parameters at bond critical points (BCPs), including electron density $\rho(r)$, its Laplacian $\nabla^2\rho(r)$, potential energy density $V(r)$, Lagrangian kinetic energy density $G(r)$, total energy density $H(r)$, and the negative ratio of kinetic to potential energy density $-G(r)/V(r)$. According to QTAIM theory, a bond path connects the nuclei of interacting atoms through a topological (3,−1) point known as the bond critical point (BCP), where the Laplacian of the electron density equals zero, $\nabla^2\rho(r) = 0$. The corresponding intermolecular graphs and topological data are illustrated in Fig. 6, and Table S11. Bond critical points arise in regions where electron density is either shared, indicating covalent bonding, or transferred,

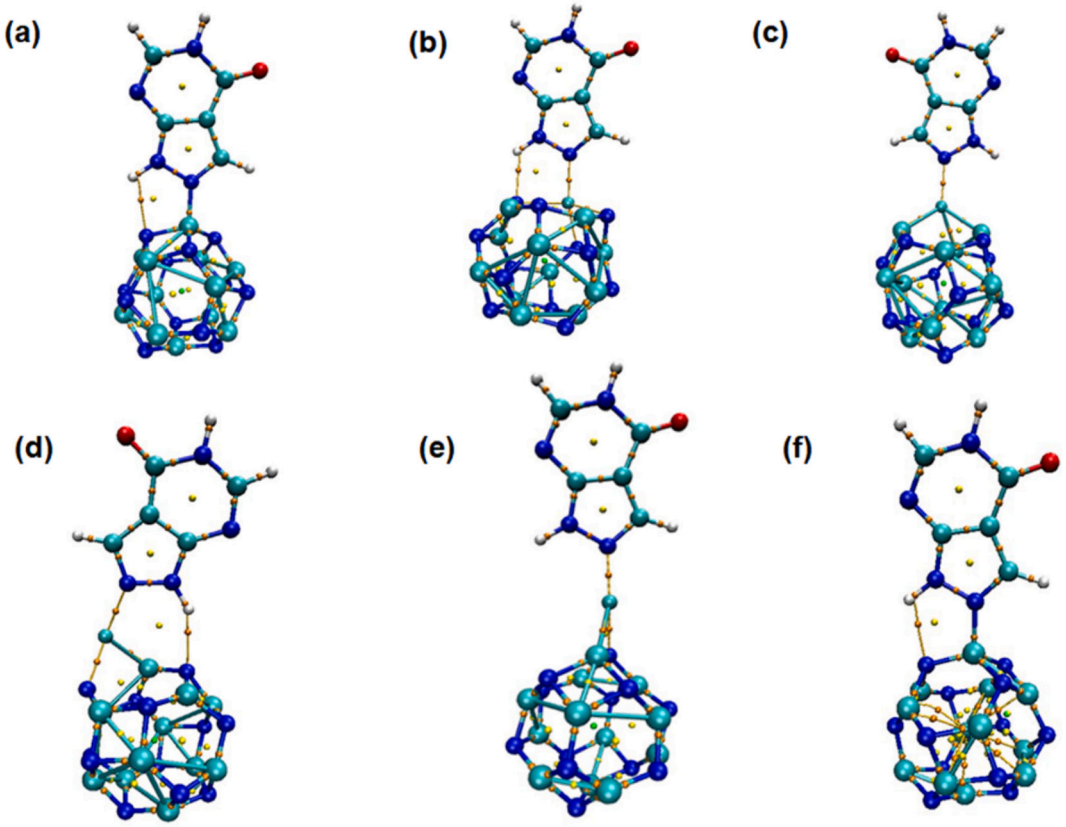

Fig. 6. QTAIM molecular graphs for all the Cu-modified $B_{12}N_{12}$–APN complexes. The yellowish points between the bonds denote bond critical points.

suggesting electrostatic interactions. The strength of intermolecular interactions can be inferred from electron density $\rho(r)$; values greater than $\rho > 0.1$ a.u. typically signify strong covalent bonding, while values below ($\rho < 0.1$ a.u.), this threshold point to weaker non-covalent interactions (NCIs).

As shown in Table S11, the electron density $\rho(r)$ values for the interactions range between 0.0201 and 0.1537 a.u. The highest $\rho(r)$ values (0.1537 and 0.1328 a.u.) observed in the $B_{12}N_{12}-$ APN and $B_{12}N_{11}Cu-$ APN complexes suggest the formation of weak covalent bonds between the APN drug and the modified $B_{12}N_{12}$ nanostructure. The table further reveals that most bond paths exhibit electron density $\rho(r)$ values below 0.1 a.u., indicating the predominance of closed-shell (non-covalent) interactions. As reported by Syzgantseva et al. [104], a positive $H(r)$ value reflects an electrostatic interaction, while a negative H(r) value signifies covalent character. As shown in the table, most of the interacting bonds exhibit negative $H(r)$ values except Cu@$B_{12}N_{12}$-APN supporting their covalent nature, which aligns with the observed electron density. Additionally, the NCI analysis reveals predominantly blue regions, suggesting the presence of repulsive interactions. Moreover, the positive values of $\nabla^2\rho(r)$ along most bond paths indicate that closed-shell interactions are dominant within the complexes. The QTAIM plots in Fig. 6 reveal that most interactions between Cu-modified $B_{12}N_{12}$ and APN occur at the doping sites involving Cu atom, while only a single interaction is observed with Cu atom for Cu@b66-APN and $B_{12}N_{12}$Cu-APN complexes. These interactions are represented by brown lines in Fig. 6. However, in the case of APN adsorption on pristine $B_{12}N_{12}$, the interactions exhibit both electrostatic and partially covalent character.

3.10. Non-covalent interactions (NCI) analysis

NCI analysis is essential for the drug design for uncovering both the intra- and intermolecular interactions between the drug and the Cu-modified $B_{12}N_{12}$ nanocages, through the study of electron density and its associated characteristics. The NCI tool was utilized to verify the types of interactions between APN drug and Cu-modified $B_{12}N_{12}$ nanocages. The reduced density gradient (RDG) plots were produced by mapping the density gradient ($S(r)$) against the electron density ($\rho(r)$), as defined by Eq. 11; [105].

$$S(r) = \frac{1}{2(3\pi^2)^{1/3}} \frac{|\nabla\rho(r)|}{[\rho(r)]^{4/3}} \tag{11}$$

Fig. 7 illustrates the 2D RDG scattered plots for the complexes under investigation. To examine weak interactions between the drug and nanocages, the NCI approach used reduced density gradient (RDG) vs electron density $\rho(sign(\lambda_2)\rho)$. The interaction between the APN drug and Cu-modified $B_{12}N_{12}$ nanocages were visualized using 2D scatter maps and 3D color-filled RDG isosurfaces, as shown in Figs. 7 and 8. Red regions with positive values suggest steric repulsion from nonbonding interactions, whereas blue regions indicate attractive interactions such as the hydrogen bonding or the dipole-dipole interactions [106]. The weak van der Waals (vdW) interaction, shown in green, indicates an electron density $sign(\lambda_2)\rho$ close to zero. In Fig. 7a–e, the spikes with low values of $sign(\lambda_2)\rho$ highlight the presence of weak interactions between the APN drug and the Cu-modified $B_{12}N_{12}$ nanocages. However, in Fig. 7f, the blue spikes appear at larger values of sign$(\lambda_2)\rho$, indicating a stronger interaction between APN and the Cu-encapsulated nanocage. The red regions represent nonbonding interaction and steric repulsion. Furthermore, the 3D color-filled RDG isosurfaces for each of the complexes under investigation are shown in Fig. 8. In every complex, disk-shaped green-red isosurfaces appear among the APN molecule and the nanocages, supporting the vertical orientation of the APN during its interaction with the nanocages. Furthermore, two disk-shaped isosurfaces are noticed inside the APN drug, formed between oxygen-hydrogen and nitrogen-hydrogen atoms, suggesting the existence of intramolecular hydrogen bonding.

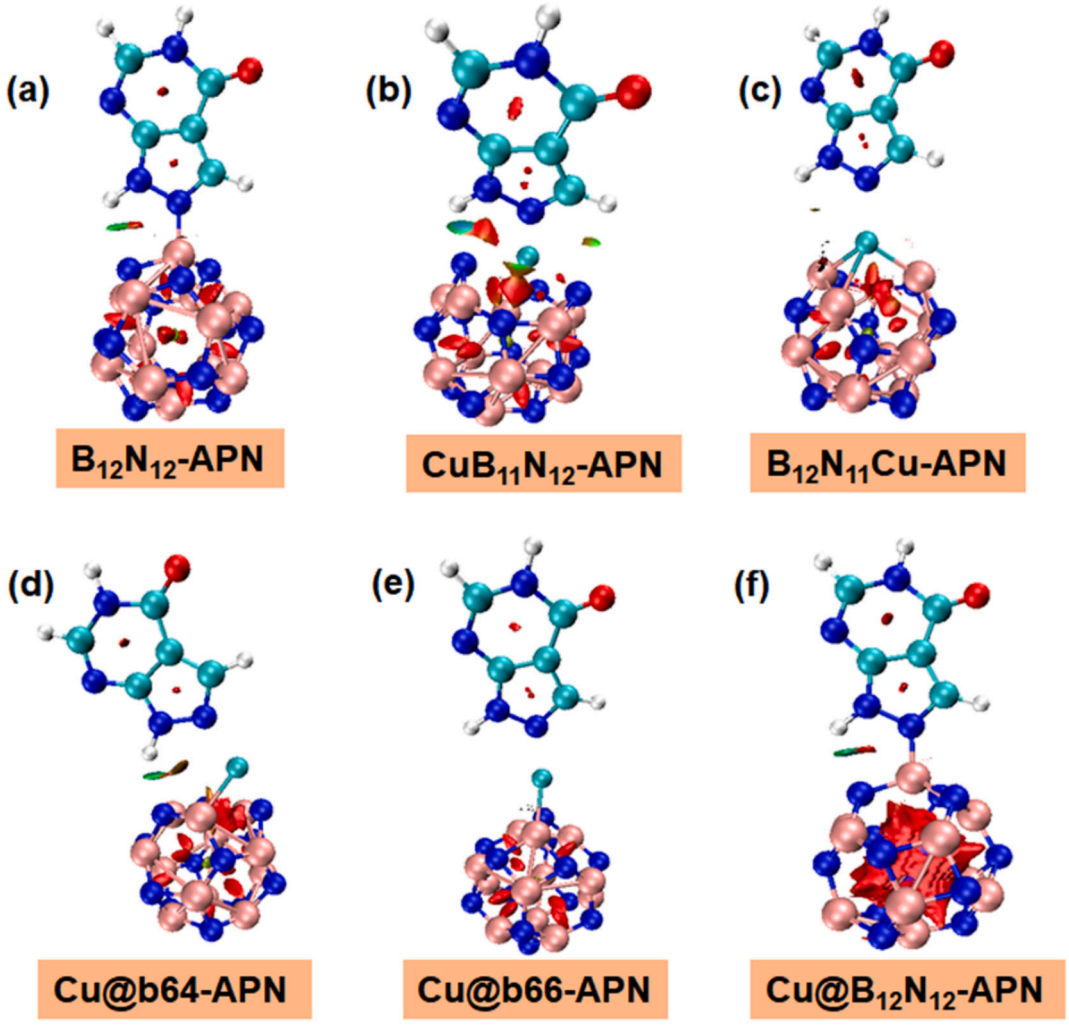

Fig. 7. 2D-RDG scatter plots.

3.11. Impacts of solvent, drug release mechanism, recovery time (τ) and molecular dynamics perspectives

We optimized Cu-modified $B_{12}N_{12}$ nanocage complexes with the APN drug in an aqueous environment using the CPCM model to explore their interaction for drug delivery. The solvent's effect on the designated complexes stability was evaluated via solvation energy calculations, as using in Eq. 12;

$$E_{sol} = E_{water} - E_{gas} \tag{12}$$

Here, E_{sol} represents the solvation energy, E_{water} denotes the energy in water phase, and E_{gas} denotes the energy in gas phase, respectively. The solvation energy of APN adsorbed onto Cu-modified nanocages increased significantly, indicating improved water solubility and potential for targeted drug delivery. Consequently, the adsorption energies in aqueous media provide key insights into the complexes' potential interactions in the human body. The computed interactions, adsorption and solvation energies are presented and summarized in Table 6.

Table 6 illustrates the stability of the Cu-modified $B_{12}N_{12}$-APN complexes in water phase, as evidenced by their favorable adsorption energies ($E^{Ads}_{solvent}$), which range from −33.18 to −45.64 kcal mol^{-1}. Additionally, the computed negative solvation energy in water phase validates the complexes' stability. Notably, the Cu@$B_{12}N_{12}$-APN encapsulated complex exhibited the highest E_{ads} value. Furthermore, the calculated dipole moments of the complexes exhibited a substantial enhancement in the aqueous phase. In the gas phase, the Cu-encapsulated Cu@$B_{12}N_{12}$-APN complex displayed the highest dipole moment at 12.36 D, followed by $B_{12}N_{11}$Cu-APN (8.85 D), Cu@b66-APN (8.70), $CuB_{11}N_{12}$-APN (8.39 D) and Cu@b64-FAV (7.89 D). In contrast, in water, the dipole moments rose to 17.25 D for the $B_{12}N_{11}$Cu-APN complex, 14.42 D for Cu@b66-APN, 13.82D for Cu@$B_{12}N_{12}$-APN, 13.78 D for Cu@b64-APN, and 11.58 D for the $CuB_{11}N_{12}$-APN complex. The enhanced dipole moment in water highlights the complexes' increased solubility in the polar solvents, signifying a substantial rise in reactivity, which is beneficial for the APN drug transport applications. The detachment of the drug from the carriers is a key factor in drug delivery, making the evaluation of the recovery time (τ) essential for evaluating the APN desorption from $B_{12}N_{12}$ nanocages. This parameter provides insights into the effectiveness of the nanocages for APN adsorption, where higher E_{ads} values are linked to longer recovery times. Desorption of APN from nanocages can limit the performance of sensors. Aligned with the research conducted by S. Thomas and M. A. Zaeem [107,108], a reduced desorption time for an adsorbent is advantageous for developing an efficient sensing device. The drug desorption recovery time (τ) from the $B_{12}N_{12}$ nanocage surface was evaluated using Eq. 13; [64].

$$\tau = \nu_0^{-1} e^{-E_{ads}/K_B T} \tag{13}$$

In the equation, the attempt frequency is denoted as ν_0, Boltzmann's constant, k_B (approximately 1.99×10^{-3} kcal mol^{-1}) [64], the adsorption energy, E_{ads}, and temperature, T in kelvin. The desorption interval of the APN drug from the Cu-decorated Cu@b66-APN complex was determined across multiple attempt frequencies at three distinct

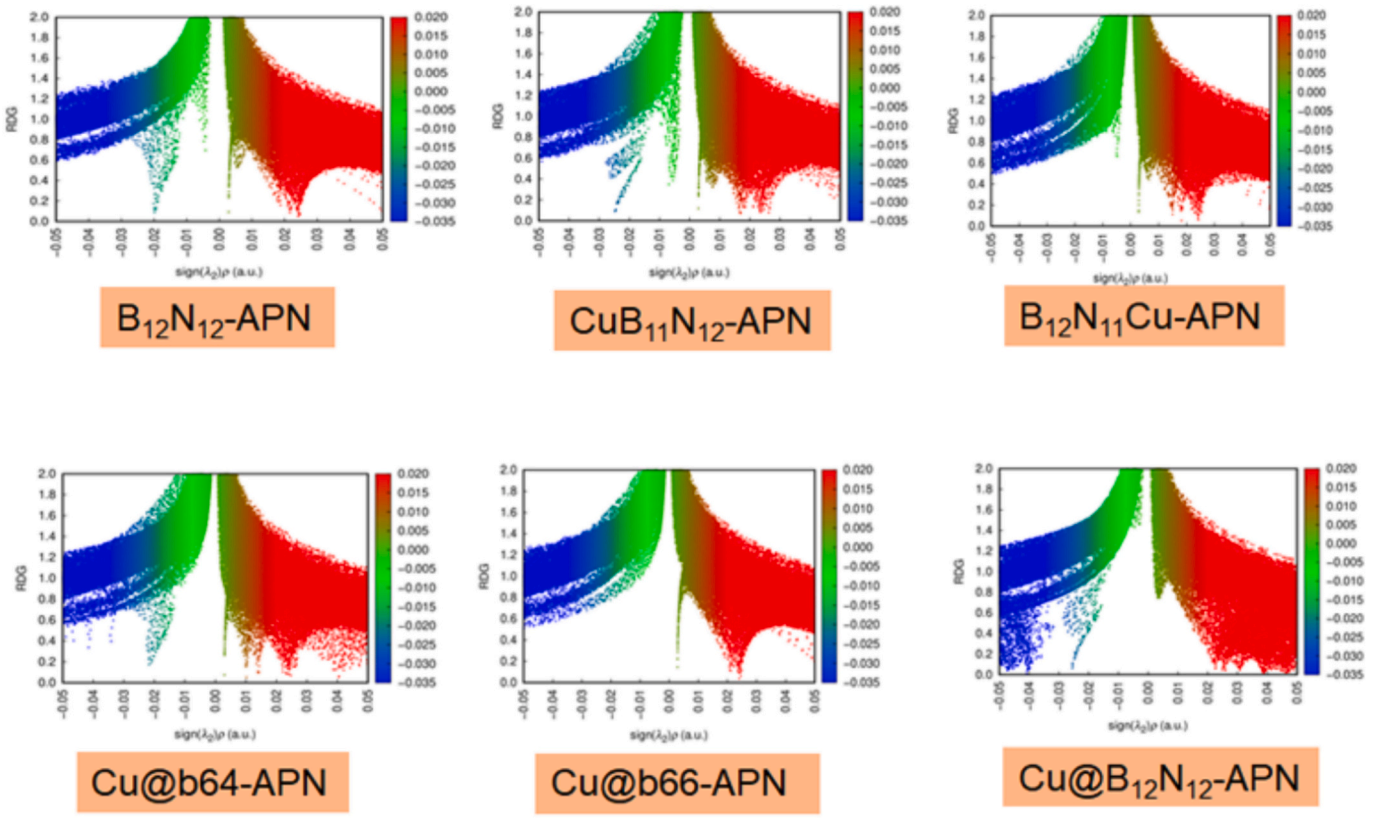

Fig. 8. 3D isosurface plots.

Table 6
The DM values in Debye, adsorption energy ($E_{ads}^{solvent}$) values in kcal mol^{-1}, HOMO energy (E_H), LUMO energy (E_L), and HOMO–LUMO energy gap (E_g) values in eV, and change in energy gap (% ΔE_g) values and recovery time (τ) for the studied systems in the water phase.

systems	DM	$E_{ads}^{solvent}$(kcal mol^{-1})	[a]ΔE_{sol} (kcal mol^{-1})	E_H(eV)	E_L(eV)	E_g(eV)	%ΔE_g
APN	4.86			−6.53	−1.04	5.49	
$B_{12}N_{12}$	0			−7.71	−0.79	6.92	
$B_{12}N_{12}$-APN	13.82	−35.79	−15.16	−7.01	−1.89	5.12	26.01
$CuB_{11}N_{12}$	3.35			−6.72	−4.78	1.94	
$CuB_{11}N_{12}$-APN	11.58	−45.64	−14.11	−6.68	−3.85	2.83	45.88
$B_{12}N_{11}Cu$	3.75			−5.10	−2.15	2.95	
$B_{12}N_{11}Cu$-APN	17.25	−33.18	−14.55	−4.78	−2.0	2.78	5.76
Cu@b64	5.50			−4.59	−1.22	3.37	
Cu@b64-APN	13.78	−39.60	−14.48	−4.33	−1.61	2.72	19.29
Cu@b66	5.34			−4.52	−1.23	3.29	
Cu@b66-APN	14.42	−35.00	−17.43	−3.90	−1.50	2.40	27.05
$Cu@B_{12}N_{12}$	4.61			−4.34	−1.38	2.96	
$Cu@B_{12}N_{12}$-APN	13.82	−43.95	−18.24	−3.91	−1.99	2.96	35.14

[a] $E_{sol} = E_{solvent}$-E_{gas}.

temperatures: 310.15 K, 398.15 K, and 498.15 K, as concisely presented in Table 7. Since desorption is the reverse of adsorption, the adsorption energy (E_{ads}) is considered to be equal to the activation energy (E_{activ}) for the desorption. However, this premise is not ideal for the sensor targeting the drug APN, leading to an unusually short recovery time of 0.16 μs. The adsorption of APN onto the nanocages $CuB_{11}N_{12}$, $B_{12}N_{11}Cu$, Cu@b64, $Cu@b_{66}$and $Cu@B_{12}N_{12}$ indicates strong physisorption (with E_{ads} ranging from −22.11 to −39.08 kcal mol^{-1}). Precisely, for 310.15 K (body temperature), the recovery time for the APN adsorption onto the Cu@b66 nanocage is calculated. The calculated recovery time of 120.01 *ms* points a moderate interaction between Cu@b66 and APN, significantly impeding spontaneous desorption of APN from Cu@b66 at room temperature, making it suitable for sensor applications. Therefore, Cu-decorated $B_{12}N_{12}$ nanocages have potential as drug delivery vehicles. The Cu@b66 nanocage demonstrates potential as a rapid-response APN detector. To assess the fluctuations in recovery time, four different attempt frequencies are used. The attempt frequencies are 3.0×10^{16} Hz

Table 7
Calculated Values of Recovery Time (τ) of APN Adsorbed Cu@b66 nanocage Using four different attempt frequencies and three different temperatures.

Attempt Frequency	Recovery Time(τ)		
	310.15 K	398.15	498.15 K
3.0×10^{16} Hz(10 nm)	120.01 ms	0.044 ms	0.16 μs
7.5×10^{14} Hz(400 nm)	4.186 s	1.76 ms	6.48 μs
3.9×10^{14} Hz(760 nm)	9.26 s	3.38 ms	12.45 μs
1.2×10^{14} Hz(2500 nm)	30.01 s	11.0 ms	40.47 μs

(ultraviolet), 7.5×10^{14} Hz (yellow light), 3.9×10^{14} Hz (yellow light), and 1.2×10^{14} Hz (yellow light), respectively [109]. The recovery times for Cu@b66-APN varied from 0.16 μs to 30.01 s over varying frequencies and temperature ranges (as shown detailed as Table 7). Specifically, at the 310.15 K(body temperature) and the frequency 3.0×10^{16} Hz, the recovery time for the complex Cu@b66 (120.01 *ms*) highlights its potential use, especially as an APN drug carrier. We also modeled the drug uptake and the release dynamics under physiological conditions by placing the $B_{12}N_{12}$-APN and Cu@b66-APN complexes in both water and acidic environments.

We further investigated the pH-responsive behavior of the system by performing protonation simulations at the N36 site of APN in the Cu@b66–APN complex. These simulations mimic the acidic tumor microenvironment (pH < 6) in contrast to physiological pH conditions (7.35–7.45). As shown in Fig. S3, the Cu—N bond length increases from 1.87 Å to 2.99 Å under acidic conditions, indicating a notable weakening of the interaction between APN and Cu@b66. This result is further supported by adsorption energy calculations, where the E_{ads} value significantly decreased from −22.11 kcal mol^{-1}, confirming the pH-triggered release of APN from the Cu@b66 nanocarrier in tumor-like environments.

To incorporate bulk solvent interactions, we employed CPCM model, where the solvent energy is calculated as the energy difference between the system insolvent and gas phase. Variations in pH between the target cells and the normal cells can initiate the release of the drug; therefore, the nitrogen atom of the APN drug was protonated under the acidic conditions in both the complexes, as depicted in in Fig. S4. DFT simulations were conducted to model the drug release process from the $B_{12}N_{12}$ and Cu@b66 nanocages APN drug complexes in acidic conditions, assessing their feasibility as an effective drug delivery systems [83]. Furthermore, four water molecules were added at these compound's binding sites to directly examine the solvent effects. The binding energies between the water and the nanocages were computed using the formula $E_{ads(H2O-BN)} = \left(E_{H2O/BN} - (E_{H2O} + E_{BN}) + E_{BSSE}\right)/4$. Thus, the solvent energies, water-$B_{12}N_{12}$ nanocage adsorption energies, and the adsorption energies of the complexes $B_{12}N_{12}$-APN and Cu@b66-APN were summarized in Table S12. The binding energies with water molecules and the $B_{12}N_{12}$, as well as Cu@b66 nanocages, are much weaker compared to those among APN drug and the nanocages, suggesting that the drug APN adsorption onto these nanocages are minimally influenced by the surrounded water molecules. The calculated aqueous and gas phases' negative adsorption energies suggest that drug binding to $B_{12}N_{12}$ nanocages is favorable and spontaneous.

As depicted in Fig. 9a, the system exhibits minimal energy fluctuations (~0.05 Eh) over 400 fs, indicating stable behavior throughout the molecular dynamics trajectory. These slight variations are attributed to minor shifts in the positioning of the APN molecule on the Cu@b66 nanocage surface, while the drug remains consistently adsorbed and the nanocage structure remains intact. Fig. 9b shows the final configuration after 400 fs, confirming that the APN molecule remains bound even in an aqueous environment. This outcome highlights the system's resistance to hydration-induced desorption, demonstrating a strong and stable interaction between APN and the Cu@b66 nanocage under dynamic conditions. Molecular dynamics simulation is a widely accepted technique for assessing the dynamic stability of nanostructured drug delivery systems [110,111].

To evaluate the stability and interactions between the drug and nanocages, ADMP dynamics simulations were performed on the most effective drug-adsorbent nanocage systems at room temperature (300*K*) in an aqueous environment. Conducted over a 1000 fs trajectory with a 0.2 fs step size, the simulations showed minimal total energy fluctuations, with no evidence of bond dissociation or fragment separation (as depicted in Figs. 10 and S5). These results highlight the nanocages' strong chemical affinity and stability, underscoring their potential as effective carriers for the APN drug in biological or aqueous environments.

4. Conclusions

This research explored the feasibility of Cu-modified $B_{12}N_{12}$ nanocages ($CuB_{11}N_{12}$, $B_{12}N_{11}Cu$, Cu@b64, Cu@b66 and the Cu@$B_{12}N_{12}$) as transporters for the APN drug through DFT computations. Key parameters, including the adsorption energy, electronic properties, dipole moments, thermodynamic properties (ΔH and ΔG), PDOS, and quantum molecular descriptors, were systematically evaluated. The negative adsorption energies in both gas (−22.11 to −39.08 kcal mol^{-1}) and solvent phases (−33.18 to −45.64 kcal mol^{-1}) confirm spontaneous and thermodynamically favorable drug binding. Cu-decoration enhanced dipole moments in gas phase from (1.71 D to 2.93 D) compared to pristine $B_{12}N_{12}$. Upon APN adsorption dipole moment changes in both gas phase (7.89 to 12.36 D) and solvent phases (11.58–17.25 D) improving aqueous-phase adsorption stability. The Cu@b64 and Cu@b66 systems showed significant HOMO–LUMO gap reductions, from 3.05 → 2.28 eV and 3.35 → 1.40 eV, respectively, indicating enhanced reactivity. Cu-modified $B_{12}N_{12}$ nanocages, particularly **Cu@b66,** demonstrated superior APN adsorption performance, with **energy gap reductions of 58.21 %** upon drug loading. PDOS and NBO results revealed notable charge transfer (up to 0.35 |e|) from APN to the nanocages, while QTAIM and NCI analysis confirmed predominant vdW-driven interactions, enabling reversible adsorption. Acidic conditions facilitated APN release via protonation, suggesting pH-responsive delivery potential. Among all candidates, Cu@b66 exhibited the shortest recovery time (~120.01 *ms*), making it the most efficient candidate for APN delivery. This research offers a concrete theoretical framework for the design and advancement of $B_{12}N_{12}$ nanocages as potent drug delivery vehicles.

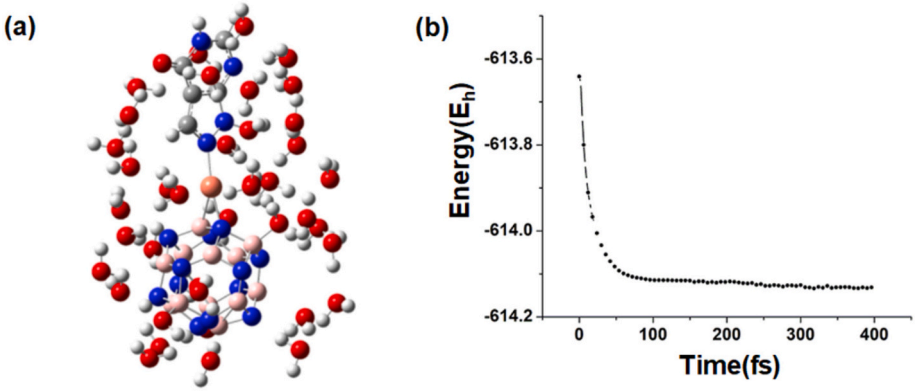

Fig. 9. (a) Optimized structures of APN adsorption on the Cu@b66-APN nanocage surrounded by 40 H_2O molecules, (b) molecular dynamics trajectories.

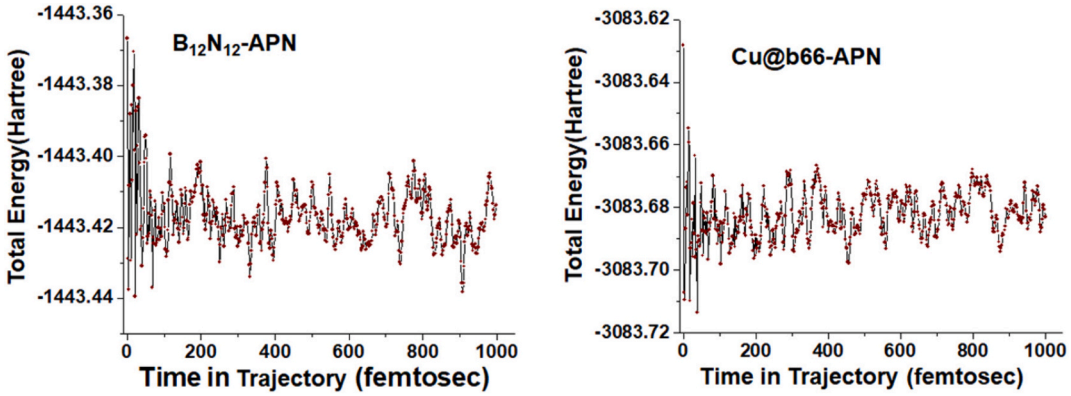

Fig. 10. ADMP molecular dynamics trajectories for 1000 fs at B3LYP-GD3(BJ)/6-31G(d,p) level of theory.

CRediT authorship contribution statement

Mohammad A. Matin: Writing – review & editing, Writing – original draft, Investigation, Funding acquisition, Formal analysis, Data curation, Conceptualization. **Md. Abdur Rahman:** Visualization, Formal analysis. **Joyanta K. Saha:** Writing – review & editing, Visualization. **Joonkyung Jang:** Writing – review & editing, Funding acquisition, Conceptualization.

Declaration of competing interest

The authors declare that they have no known competing financial interests or personal relationships that could have appeared to influence the work reported in this paper.

Acknowledgements

The authors sincerely thank the Computing Research Laboratory, CARS, DU and Computational Nanochemistry Laboratory, Pusan National University, South Korea for providing the high computational power for this study.

Appendix A. Supplementary data

Supplementary data to this article can be found online at https://doi.org/10.1016/j.molliq.2025.128749.

Data availability

The data that has been used is confidential.

References

[1] T.-F. Tsai, T.-Y. Yeh, Am. J. Clin. Dermatol. 11 (2010) 225.
[2] G.B. Elion, Science (New York, N.Y.) 244 (1989) 41.
[3] G.B. Elion, W.H. Lange, G.H. Hitchings, J. Am. Chem. Soc. 78 (1956) 2858.
[4] D.P. Chong, Can. J. Chem. 91 (2013) 637.
[5] P. Pacher, A. Nivorozhkin, C. Szabó, Pharmacological reviews 58 (2006) 87.
[6] K. Turnheim, P. Krivanek, R. Oberbauer, British journal of clinical pharmacology 48 (1999) 501.
[7] A. Šmelcerović, K. Tomović, Ž. Šmelcerović, Ž. Petronijević, G. Kocić, T. Tomašič, Ž. Jakopin, M. Anderluh, Eur. J. Med. Chem. 135 (2017) 491.
[8] M. Gorrie, M. Beaman, A. Nicholls, P. Backwell, BMJ (Clinical research ed.) 308 (1994) 113.
[9] W.H. Chung, C.W. Wang, R.L. Dao, The Journal of dermatology 43 (2016) 758.
[10] S. Halevy, P.D. Ghislain, M. Mockenhaupt, J.P. Fagot, J.N. Bouwes Bavinck, A. Sidoroff, L. Naldi, A. Dunant, C. Viboud, J.C. Roujeau, Journal of the American Academy of Dermatology 58 (2008) 25.
[11] M. Mlaouah, B. Tangour, M. El Khalifi, T. Gharbi, F. Picaud, J. Mol. Model. 24 (2018) 102.
[12] N. Aminu, I. Bello, N.M. Umar, N. Tanko, A. Aminu, M.M. Audu, J. Drug Delivery Sci. Technol. 60 (2020) 101961.
[13] V. Nagarajan, R. Chandiramouli, Comput. Theor. Chem. 1167 (2019) 112590.
[14] Q. Weng, B. Wang, X. Wang, N. Hanagata, X. Li, D. Liu, X. Wang, X. Jiang, Y. Bando, D. Golberg, ACS Nano 8 (2014) 6123.
[15] M. Nasrollahzadeh, S.M. Sajadi, M. Sajjadi, Z. Issaabadi, in: M. Nasrollahzadeh, S. M. Sajadi, M. Sajjadi, Z. Issaabadi, M. Atarod (Eds.), Interface Science and Technology, Elsevier, 2019, pp. 1–27.
[16] S.S. Dongre, S.R.C. Hunsur Ravikumar, L.C.R.G. Balakrishna, Adv. Mater. Interfaces 9 (2022) 2200442.
[17] Z.-Q. Feng, K. Yan, J. Li, X. Xu, T. Yuan, T. Wang, J. Zheng, Mater. Sci. Eng. C 104 (2019) 110001.
[18] S. Ding, W. Gu, J. Mol. Liq. 345 (2022) 117041.
[19] S. Patel, P. Patel, D. Chodvadiya, N.N. Som, P.K. Jha, J. Mol. Liq. 352 (2022) 118702.
[20] H. Zhu, C. Zhao, Q. Cai, X. Fu, F.R. Sheykhahmad, Inorg. Chem. Commun. 114 (2020) 107808.
[21] D. Golberg, Y. Bando, O. Stéphan, K. Kurashima, Appl. Phys. Lett. 73 (1998) 2441.
[22] N.G. Chopra, R.J. Luyken, K. Cherrey, V.H. Crespi, M.L. Cohen, S.G. Louie, A. Zettl, Science (New York, N.Y.) 269 (1995) 966.
[23] S.K. Vashist, J.H.T. Luong, Carbon 84 (2015) 519.
[24] H. Xu, X. Tu, G. Fan, Q. Wang, X. Wang, X. Chu, J. Mol. Liq. 318 (2020) 114315.
[25] F. Jensen, H. Toftlund, Chem. Phys. Lett. 201 (1993) 89.
[26] M. Shamima Khanom, M. Rakib Hossain, K. Zahirul Islam, M. Abul Hossain, F. Ahmed, Comput. Theor. Chem. 1216 (2022) 113869.
[27] S. Hussain, R. Hussain, M.Y. Mehboob, S.A.S. Chatha, A.I. Hussain, A. Umar, M. U. Khan, M. Ahmed, M. Adnan, K. Ayub, ACS Omega 5 (2020) 7641.
[28] H.Y. Ammar, H.M. Badran, K.M. Eid, Mater. Today Commun. 25 (2020) 101681.
[29] W. Xie, J. Wang, J. Wang, X. Wu, Z. Wang, R.-Q. Zhang, J. Phys. Chem. C 124 (2020) 3881.
[30] G. Seifert, P.W. Fowler, D. Mitchell, D. Porezag, T. Frauenheim, Chem. Phys. Lett. 268 (1997) 352.
[31] T. Oku, A. Nishiwaki, I. Narita, Sci. Technol. Adv. Mater. 5 (2004) 635.
[32] D.L. Strout, J. Phys. Chem. A 104 (2000) 3364.
[33] T. Oku, A. Nishiwaki, I. Narita, Solid State Commun. 130 (2004) 171.
[34] T. Oku, Energies 8 (2015) 319.
[35] Y.-C. Zhu, Y. Bando, L.-W. Yin, D. Golberg, Chem. Eur. J. 10 (2004) 3667.
[36] İ. Muz, S. Alaei, M. Kurban, Mater. Today Commun. 27 (2021) 102252.
[37] İ. Muz, F. Göktaş, M. Kurban, Chem. Phys. 539 (2020) 110929.
[38] S. Lin, X. Wang, Y. Yang, X. Meng, Y. Qu, Y.-Q. Li, M. Zhao, X. Liu, W. Li, J. Phys. D: Appl. Phys. 55 (2022) 295401.
[39] A. Merlo, V.R.S.S. Mokkapati, S. Pandit, I. Mijakovic, Biomater. Sci. 6 (2018) 2298.
[40] M.H. Miah, M.R. Hossain, M.S. Islam, T. Ferdous, F. Ahmed, RSC Adv. 11 (2021) 38457.
[41] Y. Cao, A. Khan, H. Balakheyli, A.N.K. Lup, M. Ramezani Taghartapeh, H. Mirzaei, S. Reza Khandoozi, A. Soltani, M. Aghaei, F. Heidari, S.M. Sarkar, A. B. Albadarin, Arab. J. Chem. 14 (2021) 103200.
[42] M.K. Hazrati, N.L. Hadipour, Phys. Lett. A 380 (2016) 937.
[43] D.V. Shtansky, K.L. Firestein, D.V. Golberg, Nanoscale 10 (2018) 17477.
[44] A. Soltani, A. Sousaraei, M. Bezi Javan, M. Eskandari, H. Balakheyli, New J. Chem. 40 (2016) 7018.
[45] M.A.A. Ibrahim, A.-S.S.M. Rady, P.A. Sidhom, M.E.S. Soliman, S. Khan, M.A. El-Tayeb, A.M.M. Abdelbacki, T. Shoeib, L.A. Mohamed, Chem. Phys. Lett. 857 (2024) 141729.
[46] M.J. Saadh, M. Mirzaei, Z.S. Ghnim, S.A. Mosaddad, M.M. Salem-Bekhit, Comput. Theor. Chem. 1237 (2024) 114664.
[47] R. Guo, Q. Liu, W. Wang, R. Tayebee, F. Mollania, J. Mol. Liq. 325 (2021) 114798.
[48] M. Kurban, İ. Muz, J. Mol. Liq. 309 (2020) 113209.
[49] S. Wu, L. Li, Q. Liang, H. Gao, T. Tang, Y. Tang, New J. Chem. 47 (2023) 21743.
[50] N. Abdolahi, P. Singla, A. Soltani, M. Javan, M. Aghaei, F. Heidari, S. Sedighi, Physica E: Low-dimensional Syst. Nanostruct. 124 (2020) 114296.
[51] M. Sadat Mussavi, S. Hosseini, J. Mol. Liq. 395 (2024) 123900.
[52] X. Yao, J. Mu, Y. Zheng, J. Wu, W. Zhu, K. Wang, Colloids Surface A 678 (2023) 132481.

[53] S.U.D. Shamim, M.H. Miah, M.R. Hossain, M.M. Hasan, M.K. Hossain, M. A. Hossain, F. Ahmed, Physica E: Low-dimensional Syst. Nanostruct. 136 (2022) 115027.
[54] Y. Cao, A. Khan, F. Ghorbani, H. Mirzaei, P. Singla, H. Balakheyli, A. Soltani, M. Aghaei, Z. Azmoodeh, M. Aarabi, S. Tavassoli, J. Mol. Liq. 339 (2021) 116678.
[55] A. Soltani, M.R. Taghartapeh, V. Erfani-Moghadam, M.B. Javan, F. Heidari, M. Aghaei, P.J. Mahon, Mater. Sci. Eng. C92 (2018) 216.
[56] İ. Muz, Mater. Today Commun. 31 (2022) 103798.
[57] Y. Lai, T.J. Al-Musawi, U. Abdul-Reda Hussein, I. Waleed, H. Hassan Ahmed, A. Qasim Khallawi, K. Majid Alsaraf, M. Asiri, M. Abosaooda, H.O. Alsaab, J. Mol. Liq. 384 (2023) 122260.
[58] M.R. Hossain, M.M. Hasan, M. Nishat, E.A. Noor, F. Ahmed, T. Ferdous, M. A. Hossain, J. Mol. Liq. 323 (2021) 114627.
[59] P. Dhali, A.K.M.A. Hossain, J. Mol. Liq. 396 (2024) 124051.
[60] G. Mehraein, M. Rezaei-Sameti, E. Asgary, M. Aghamohammadi, J. Mol. Struct. 1248 (2022) 131478.
[61] M. Suliman, M. Hadi Kzar, A.S.M. Juma, I. Abbas Ali, Y. Yasin, N. Hassan Sayyid, A. Taan Alkhafaji, A.J. Kadhim, M.M. Abid, A. Hussien Alawadi, A. Alsalamy, J. Kaur, E. Tazikeh-Lemeski, S. Moazen Rad, A. Soltani, J. Mol. Liq. 395 (2024) 123816.
[62] M. Khaleghian, M. Sheikhi, S. Shahab, S. Kaviani, Comput. Theor. Chem. 1237 (2024) 114616.
[63] M.A. Matin, M. Alauddin, M.M. Islam, J. Mol. Liq. 407 (2024) 125244.
[64] M.A. Matin, J.K. Saha, T. Debnath, J. Jang, J. Mol. Liq. 414 (2024) 125999.
[65] S. Kaviani, S. Shahab, M. Sheikhi, Physica E: Low-dimensional Syst. Nanostruct. 126 (2021) 114473.
[66] A.A. Piya, A.K.M.A. Hossain, RSC Advan. 13 (2023) 27309.
[67] İ. Muz, M. Kurban, J. Mol. Liq. 335 (2021) 116181.
[68] Z.M. Shabavi, E. Shakerzadeh, T. Yadav, E. Tahmasebi, S. Kaviani, E.C. Anota, Comput. Theor. Chem. 1234 (2024) 114535.
[69] M.A.A. Ibrahim, A.-S.S.M. Rady, P.A. Sidhom, S.R.M. Sayed, K.E. Ibrahim, A. M. Awad, T. Shoeib, L.A. Mohamed, ACS Omega 9 (2024) 25203.
[70] A. Maleki, Struct. Chem. 33 (2022) 323.
[71] M. Pishnamazi, S.M. Alshahrani, H. Faris Alotaibi, J. Mol. Liq. 410 (2024) 125541.
[72] G. Jouonang Létché, A.D. Tamafo Fouegue, V.D.P. Zoua, R. Abdoul Ntieche, G. B. Noumi, Mater. Sci. Semicond. 185 (2025) 108980.
[73] S. Bibi, S. Ur-rehman, L. Khalid, I.A. Bhatti, H.N. Bhatti, J. Iqbal, F.Q. Bai, H.-X. Zhang, RSC Advances 12 (2022) 2873.
[74] S. Ketabi, S. Shalmashi, S. Hallajian, BMC Chemistry 17 (2023) 169.
[75] A.J. Bin Iqbal, R. Shahriar, A. Zubair, Nanoscale Adv. 6 (2024) 2968.
[76] Y. Zhang, Y. Luo, L. Tang, M.E.J. Hu, J. Mol. Liq. 393 (2024) 123607.
[77] A.L. Pereira Silva, J.D.J.G. Varela Júnior, Inorg. Chem. 62 (2023) 1926.
[78] M.J. Frisch, G.W. Trucks, H.B. Schlegel, G.E. Scuseria, M.A. Robb, J. R. Cheeseman, G. Scalmani, V. Barone, G.A. Petersson, H. Nakatsuji, X. Li, M. Caricato, A.V. Marenich, J. Bloino, B.G. Janesko, R. Gomperts, B. Mennucci, H. P. Hratchian, J.V. Ortiz, A.F. Izmaylov, J.L. Sonnenberg, F. Ding Williams, F. Lipparini, F. Egidi, J. Goings, B. Peng, A. Petrone, T. Henderson, D. Ranasinghe, V.G. Zakrzewski, J. Gao, N. Rega, G. Zheng, W. Liang, M. Hada, M. Ehara, K. Toyota, R. Fukuda, J. Hasegawa, M. Ishida, T. Nakajima, Y. Honda, O. Kitao, H. Nakai, T. Vreven, K. Throssell, J.A. Montgomery Jr., J.E. Peralta, F. Ogliaro, M. J. Bearpark, J.J. Heyd, E.N. Brothers, K.N. Kudin, V.N. Staroverov, T.A. Keith, R. Kobayashi, J. Normand, K. Raghavachari, A.P. Rendell, J.C. Burant, S. S. Iyengar, J. Tomasi, M. Cossi, J.M. Millam, M. Klene, C. Adamo, R. Cammi, J. W. Ochterski, R.L. Martin, K. Morokuma, O. Farkas, J.B. Foresman, D.J. Fox, Wallingford, CT, 2016.
[79] S.F. Boys, F. Bernardi, Mol. Phys. 19 (1970) 553.
[80] J. Tomasi, B. Mennucci, R. Cammi, Chem. Rev. 105 (2005) 2999.
[81] N.M. O'boyle, A.L. Tenderholt, K.M. Langner, J. Comput. Chem. 29 (2008) 839.
[82] T. Lu, F. Chen, J. Comput. Chem. 33 (2012) 580.
[83] M. Kanamala, W.R. Wilson, M. Yang, B.D. Palmer, Z. Wu, Biomaterial 85 (2016) 152.
[84] E. Shakerzadeh, Comput. Theor. Chem. 1202 (2021) 113339.
[85] M.J. Saadh, S. Abdalkareem Jasim, D.T. Castañeda Ortiz, A. Kumar, A. Kumar, P. Ghildiyal, E. Anad Jabouri, I. Habeeb Naser, K. Muzammil, Inorg. Chem. Commun. 162 (2024) 112187.
[86] H.M. Badran, K.M. Eid, H.Y. Ammar, J. Phys. Chem. Solids 141 (2020) 109399.
[87] S. Larki, E. Shakerzadeh, E.C. Anota, R. Behjatmanesh-Ardakani, Chem. Phys. 526 (2019) 110424.
[88] M.R.S.A. Janjua, Inorg. Chem. 60 (2021) 10837.
[89] Z. Zhao, Z. Li, Q. Wang, Chem. Phys. Lett. 739 (2020) 136922.
[90] A. Soltani, E. Tazikeh-Lemeski, M.B. Javan, J. Mol. Liq. 297 (2020) 111894.
[91] N. de Sousa Sousa, A.L.P. Silva, A.C.A. Silva, J. de Jesus Gomes, Varela Júnior, J. Nanopart. Res. 25 (2023) 248.
[92] L. Zhang, X. Cheng, X.-H. Li, J.-H. Chen, W.-M. Sun, J. Mol. Liq. 360 (2022) 119388.
[93] S. Thomas, M. Asle Zaeem, Appl., Surf. Sci. 563 (2021) 150232.
[94] T. Kaewmaraya, L. Ngamwongwan, P. Moontragoon, A. Karton, T. Hussain, J. Phys. Chem. C122 (2018) 20186.
[95] T. Kaewmaraya, L. Ngamwongwan, P. Moontragoon, W. Jarernboon, D. Singh, R. Ahuja, A. Karton, T. Hussain, J. Hazard. Mater. 401 (2021) 123340.
[96] İ. Muz, F. Göktaş, M. Kurban, Theor. Chem. Acc. 139 (2020) 23.
[97] S.S. Li, in: S.S. Li (Ed.), Semiconductor Physical Electronics, Springer, New York, New York, NY, 2006, pp. 211–245.
[98] R.G. Pearson, Inorg. Chem. 27 (1988) 734.
[99] R.G. Parr, L.V. Szentpály, S. Liu, J. Am. Chem. Soc. 121 (1999) 1922.
[100] F. Mollania, N.L. Hadipour, N. Mollania, J. Biotechnol. 308 (2020) 40.
[101] E. Mirhaji, M. Afshar, S. Rezvani, M. Yoosefian, J. Mol. Liq. 271 (2018) 151.
[102] J.P. Cachaneski-Lopes, A. Batagin-Neto, J. Nanostruct. Chem. 12 (2022) 141.
[103] S. Dushman, Rev. Mod. Phys. 2 (1930) 381.
[104] O.A. Syzgantseva, V. Tognetti, L. Joubert, J. Phys. Chem. A117 (2013) 8969.
[105] E.R. Johnson, S. Keinan, P. Mori-Sánchez, J. Contreras-García, A.J. Cohen, W. Yang, J. Am. Chem. Soc. 132 (2010) 6498.
[106] J.K. Saha, J. Raihan, M.A. Matin, J. Jang, Struct. Chem. 35 (2024) 297.
[107] S. Thomas, M. Asle Zaeem, Adv., Theor. Simul. 4 (2021) 2000250.
[108] S. Thomas, V. Kumar, D.R. Roy, M.A. Zaeem, A.C.S. Appl, Nano Mater. 3 (2020) 10073.
[109] D. Paul, A. Vaidyanathan, U. Sarkar, B. Chakraborty, Struct. Chem. 32 (2021) 2259.
[110] N. de Sousa Sousa, J. de Jesus Gomes, Varela Junior, Langmuir 41 (2025) 7396.
[111] N. de Sousa Sousa, R. Pereira Silva, J. de Jesus Gomes, A. Varela Júnior, Pereira Maciel, Langmuir 40 (2024) 23310.